# scientific reports



## **OPEN** Extensive electronic investigation of BMBH structure and adsorption locator on graphene with molecular dynamics of human serum albumin interaction

Walaa S. S. Alblozy¹, Doaa S. El Sayed²™ & Refaat M. Mahfouz¹™

A comprehensive electronic investigation of Bambuterol Hydrochloride (BMBH) was conducted to explore its structural properties, adsorption behavior on graphene, molecular docking interactions, and molecular dynamics perturbations. FT-IR and XRD characteristics were performed to support the structural identity. Geometry optimization and theoretical calculations were carried out to study the structural and electronic properties of BMBH. The nature of hydrogen and halogen bonding interactions was analyzed using natural bond orbital (NBO) analysis, atoms in molecules (AIM) theory, and Reduced Density Gradient (RDG) analysis. Additionally, electron localization function (ELF) analysis provided deeper insights into the chemical bonding characteristics of BMB. Adsorption locator modelling was involved to allow activated carbon-carriers for sustained and controlled drug release, which helps maintain therapeutic drug levels in the body over time, reducing the frequency of administration. Molecular docking analysis was performed to assess the interaction of BMBH with key biological targets, revealing its potential pharmacological relevance. The inhibitory interaction of BMB with the butyrylcholinesterase enzyme, which is a major cause of dementia and Alzheimer's disease, has been investigated based on molecular modelling. In addition to that the interaction between BMB and Human Serum Albumin (HSA) was assessed using molecular Docking and Molecular dynamics studies to investigate its transportation and bioavailability. Additionally, molecular dynamics simulations were employed to evaluate the structural perturbations and dynamic behaviour of the BMBH/graphene and BMB/target complexes over time. The study offers a detailed understanding of the electronic and interactional properties of BMB, contributing to its potential applications in nanomaterial-based drug delivery and therapeutic interventions.

Keywords BMBH drug, Computational study, DFT calculations, Graphene adsorption, Molecular docking, Dynamic simulation

. e primary goal of scientists and dosage form designers is to improve the safety of a drug molecule while preserving its therapeutic e.. acyl-3. Recent advancements in Novel Drug Delivery Systems (NDDS) aim to achieve this by developing dosage forms that are easy to administer, ultimately improving patient compliance. Pharmaceutical technologists have focused their e. orts on creating Fast Dissolving Drug Delivery Systems<sup>4-6</sup>. ese tablets, which rapidly disintegrate or dissolve in the mouth, are especially benefic al for children, elderly patients, those with swallowing di.. ulties, or when drinking liquids may not be feasible. Bambuterol hydrochloride is a long-acting β<sub>2</sub>-adrenergic receptor agonist (LABA) used primarily in managing asthma and chronic obstructive pulmonary disease (COPD)<sup>7,8</sup>. As a prodrug of terbutaline, it undergoes hepatic metabolism to release the active compound, providing a sustained bronchodilatory e. ect. Due to its extended half-life, bambuterol o. ers advantages over short-acting β<sub>2</sub>-agonists by reducing dosing frequency and improving patient compliance9. This research examines bambuterol hydrochloride in pulmonary medicine. It highlights its potential to improve disease control, patient adherence, and treatment outcomes for asthma and COPD. Bambuterol

<sup>1</sup>Chemistry Department, Faculty of Science, Assiut University, Assiut, Egypt. <sup>2</sup>Chemistry Department, Faculty of Science, Alexandria University, Baghdad Street, Moharam Bey, P.O. Box 21511, Alexandria, Egypt. 🖾 email: doaasaied75@yahoo.com; doaasaeed@alexu.edu.eg; rmhfouz@aun.edu.eg

hydrochloride (BMBH), chemically known as (RS)-5-(2-tert-butylamino-1-hydroxyethyl)-m-phenylene bis(dimethyl carbamate) hydrochloride (Fig. 1), is a long-acting, orally administered sympathomimetic drug with predominant adrenergic activity (\beta1-agonist). It is widely prescribed for asthma and COPD management  $^{10-12}$ . As an ester prodrug of the  $\beta^2$  adrenergic agonist terbutaline  $^{13,14}$ , bambuterol hydrochloride has been analyzed using solid-state NMR s pectroscopy, GC-MS, and potentiometric titration. Research suggests that its active enantiomer is more e. ective in treating asthma than the (S)-bambuterol hydrochloride enantiomer<sup>15</sup>. It acts as a directly acting sympathomimetic agent and primarily exhibits adrenergic activity<sup>16</sup>. As a dicarbamate ester, it remains stable pre-systemically until it reaches lung tissues, where it undergoes hydrolysis by butyrylcholinesterase to release terbutaline, the active β2 adrenergic agonist<sup>17</sup>. Applying NDDS such as SEDDS, SMEDDS, and FDTs for bambuterol hydrochloride has shown promise in addressing its bioavailability challenges, potentially leading to more e. ective asthma management strategies. SEDDS enhance drug solubility and bioavailability by self emulsifying in gastrointestinal. uids. A study formulated a solid SEDDS for BMBH, showing improved permeability and potential bioavailability. SMEDDS forms microemulsions for better drug absorption. BMBH/ SMEDDS showed stability, rapid emulsifi ation, and enhanced permeability, suggesting improved bioavailability. FDTs dissolve quickly for faster action and better compliance. BMBH/FDT with crospovidone showed the best disintegration and dissolution, suggesting improved bioavailability. NDDS like SEDDS, SMEDDS, and FDTs o. er promise for better asthma treatment<sup>18,19</sup>.

In this study, density functional theory (DFT) calculations have been employed as a robust theoretical approach to complement the experimental characterization of bambuterol hydrochloride (BMBH) and to enhance understanding of its in-vivo pharmacological interactions. Adsorption on Graphene system can give an insight into the stability of BMBH with enhancement hydrogen attraction and storage on the electron rich surface. Investigations include molecular geometry analysis, natural bond orbital (NBO) analysis, hydrogen bonding interactions, as well as AIM, ELF, RDG, and FT-IR spectroscopy studies (Fig. 1).

#### Materials and methods

All the chemicals used were of analytical grade. Spectroscopic-grade solvent ethanol (EtOH), and 5-(2-(tert-butylamino)-1-hydroxyethyl)-1,3-phenylene bis(dimethylcarbamate) hydrochloride (bambuterol hydrochloride) (purity  $\geq$  98%), were sourced from Sigma-Aldrich. Fourier transform infrared spectroscopy (FT-IR) was used to detect the functional groups of samples from 400–4000 cm<sup>-1</sup> using a Perkin Elmer spectrometer via the KBr pellet method (Spectrum One, USA). A T80 + UV/Vis double-beam spectrophotometer from PG Instruments Ltd, UK, recorded electronic absorption spectra within the 200–600 nm wavelength range. A high-resolution scanning electron microscope (HRSEM) was form. tting with EDX (JEOL, JSM [model no: 6360]). X-ray di. raction (XRD) p atterns were determined via Cu K $\alpha$  X-ray radiation (Germany,  $\lambda$ =1.540 Å, PAN analytical X'PERT PRO). e di. raction angle ( $\theta$ ), di. raction intensity (I), peak area (A), and full width at half maximum (FWHM) can be derived from the XRD spectrum<sup>20</sup> as shown in Table 1.

#### Computational details

DFT computations have been performed using the Gaussian 09 program package $^{21-23}$ . Geometry optimization and conformational analysis of the single molecule were performed using RB3LYP level (a hybrid approach that integrates Becke's three-parameter exchange functional with the Lee–Yang–Parr correlation functional) with a 6–31+G (d) basis set to achieve the optimal conditions for structural parameter calculations and ground state optimization in the gas phase. . e selected DFT calculation level was achieved because it provides a good balance between accuracy and efficiency. It performs well for organic molecules, transition states, and general thermochemical properties. It accounts for electron correlation e. ects better than pure DFT functionals.

. e dispersion-corrected DFT (DFT-D3) approach<sup>24</sup> was employed in this study to give better results for non-covalent interactions<sup>25</sup>. e frequency calculations for the optimized structure of BMBH have shown no imaginary frequencies; hence, it confi ms that they are true minima. e chemical reactivity has been predicted given the HOMO-LUMO gap and reactivity descriptors. e stability of the title compound was analyzed using natural bond order (NBO) analysis. e chemical activity was measured using molecular electrostatic potential (MEP) analysis. e activity and stability of the compound have been further investigated by the non-covalent interactions by the Multiwfn program<sup>26</sup>. Th s has been achieved through studying the atoms in molecules (AIM)

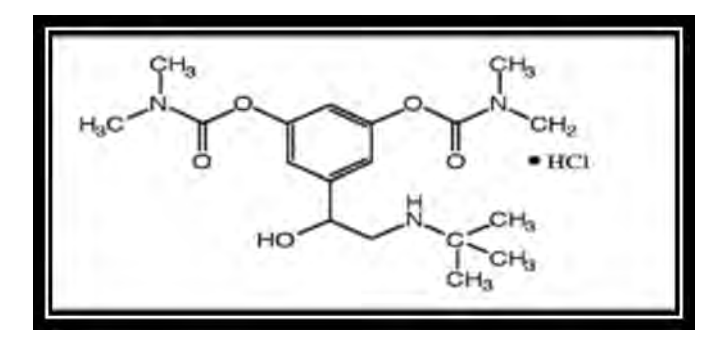


**Fig. 1.** . e molecular structure of 5-(2-(tert-butylamino)-1-hydroxyethyl)-1,3-phenylene bis(dimethylcarbamate) hydrochloride (BMBH).

Pos. (2θ°)	d-spacing (Å)	Height (cts)	FWHM Left (2θ°	Rel. Int. (%)
10.9526	8.07150	1418.61	0.0568	100.00
11.8952	7.43394	110.09	0.0709	7.76
12.4730	7.09089	74.75	0.0896	5.27
12.8175	6.90103	54.59	0.0836	3.85
16.2360	5.45491	47.31	0.0999	3.33
17.5803	5.04069	132.06	0.0994	9.31
18.0453	4.91185	25.93	0.1167	1.83
20.7065	4.28619	113.99	0.1795	8.04
20.8605	4.25489	150.54	0.1041	10.61
21.5291	4.12424	47.66	0.1404	3.36
22.1105	4.01708	48.31	0.1010	3.41
22.8845	3.88294	41.24	0.1439	2.91
23.9619	3.71073	23.64	0.2168	1.67
24.8661	3.57782	115.80	0.1710	8.16
25.1781	3.53419	222.41	0.1256	15.68
26.0731	3.41486	15.88	0.2536	1.12
26.5183	3.35853	26.42	0.1565	1.86
27.4896	3.24203	24.37	0.2696	1.72
28.6422	3.11413	49.56	0.1788	3.49
30.1908	2.95783	6.71	0.1446	0.47
32.0110	2.79368	15.77	0.4180	1.11
32.6034	2.74426	22.98	0.2521	1.62
33.4553	2.67629	84.04	0.1102	5.92
33.9935	2.63514	93.18	0.1223	6.57
34.4375	2.60218	17.01	0.2186	1.20
35.6467	2.51663	46.38	0.1381	3.27
38.2024	2.35394	13.93	0.2639	0.98
43.8222	2.06422	18.19	0.2754	1.28
45.1119	2.00816	28.59	0.3087	2.02
45.5964	1.98794	26.10	0.2033	1.84
48.1462	1.88844	10.08	0.2243	0.71
49.2849	1.84744	7.81	0.3597	0.55
55.4801	1.65492	5.76	0.5923	0.41

**Table 1**. X-ray di. raction (XRD) parameters of BMBH, including peak position ( $2\theta$ ), d-spacing, intensity (cts), full width at half maximum (FWHM), and relative intensity (%).

approach, the electron localization function, the electrostatic potential map, and the reduced-density gradient (RDG). e Gauss View 6 program<sup>27</sup> was used to enhance the visual animation to verify the normal modes.

#### Molecular docking protocol

Our study examines how BMBH binds to and inhibits BChE, potentially preventing acetylcholine degradation and improving cognitive function. Molecular modelling and visualization via molecular docking were performed where the structure of Human butyrylcholinesterase in complex with thio. avine T were obtained from the RCSB Protein Data Bank (PDB ID: 6ESY) <a href="https://www.rcsb.org/structure/6esy">https://www.rcsb.org/structure/6esy</a>. Docking protocol was validated by re-docking of the co-crystalized thio. avine T at the 297 active site of butyrylcholinesterase.

Another molecular docking analysis was conducted to elucidate the binding interactions between Human Serum Albumin (HSA) and BMBH. Docking against HSA helps assess drug binding, bioavailability, and potential interactions with natural compounds, in. uencing pharmacokinetics and e.. acy. . e three-dimensional structure of HSA, complexed with oxyphenbutazone, was retrieved from the Protein Data Bank (PDB ID: 2BXB)<sup>28</sup> at https://www.rcsb.org/structure/2bxb. Salbutamol (Albuterol), a commonly used  $\beta_2$  agonist was also docked against HAS for the sake of comparing their bioavailability including their distribution, and duration of action.

For receptors preparation, all crystallographic water molecules and co-crystallized ligands were removed using AutoDock Vina. Subsequently, polar hydrogen atoms were incorporated, and the receptor structures were subjected to energy minimization using the prepare\_receptor4.py script from AutoDockTools (ADT, v1.5.6)<sup>29,50</sup>. Kollman-united atom charges were assigned, and the processed receptor structure was stored in PDBQT format<sup>31</sup>.

Ligand preparation involved the conversion of BMBH into a docking-compatible format using the prepare\_ligand4.py script from ADT, followed by storage in PDBQT format. . e docking grid was centred at the co-

crystallized ligand-binding pocket of HSA, with dimensions set to 40 Å along each Cartesian axis (x, y, z). Docking simulations were conducted using the Lamarckian Genetic Algorithm with parameters set to 2,500,000 energy evaluations, 100 independent runs, and a population size of  $150^{32}$ . Docking conformations within 3 kcal/mol of the lowest energy pose were selected. Molecular interactions were visualized in BIOVIA Discovery Studio Visualizer 2021, generating 2D maps<sup>33</sup>.

#### Molecular dynamics simulation

. e interaction stability of BMBH within the HSA active site was further investigated through molecular dynamics (MD) simulations utilizing GROMACS-2023.1<sup>34</sup>. . e CHARMM36 force fi ld was implemented to parameterize the protein topology, while ligand topology parameters were derived via the CGenFF server<sup>35,36</sup>. To uphold periodic boundary conditions and mitigate edge e. ects, the system was solvated in a do decahedral unit cell with a 10 Å bu. er. Sodium and chloride ions were introduced to ensure electrostatic neutrality. Energy minimization was executed using the steepest descent algorithm with a force convergence criterion of 10.0 kJ/mol, iterating up to 50,000 steps to eliminate steric hindrances. Th s process was followed by two equilibration phases: the NVT (isothermal-isochoric) and NPT (isothermal-isobaric) ensembles, each conducted for 50,000 steps (10 picoseconds), employing a modifi d Berendsen thermostat and a leap-frog integration scheme. Subsequently, the production MD simulation was performed for 200 ns with a 2-femtosecond integration time step.

### Results and discussion FT-IR spectra

. e assignments were completed over the estimated range of wavenumber as shown in Fig. 2. A broadband was observed at  $3046~\rm cm^{-1}$ , this can be attributed to the OH group. Meanwhile, the band at  $2875~\rm cm^{-1}$  was attributed to the N–H group of secondary amines. . e later band shift may be due to the intramolecular H-bond inclusion. Other observed bands at  $2448~\rm cm^{-1}$  and  $2358~\rm cm^{-1}$  appeared for C–H aromatic and C–H aliphatic groups. A sharp band appeared at  $1700~\rm cm^{-1}$ , was attributed to the C=O group.

. e molecule consists of 57 atoms, resulting in a total of 165 vibrational modes. . ese modes are distributed among di. erent symmetry species based on the  $C_2$  point symmetry of the molecule, which has a non-planar structure. . e vibrations are categorized as either in-plane or out-of-plane. . e calculated wavenumbers are generally higher than the experimental values for most normal modes. This discrepancy is due to vibrational di. erences. . eoretical calculations use the gas phase, while experiments use the solid state. Additionally, experimental values correspond to anharmonic wavenumbers, while the computed values are harmonic. To account for this anharmonicity, a scaling factor of 0.9608 is applied to the computed wavenumbers. . e methyl groups play a crucial role in the vibrational spectrum of BMBH, as the molecule contains seven methyl groups. . erefore, the assignment of methyl group vibrations is examined in detail. Each methyl group has nine vibrational modes: two asymmetric stretches, one symmetric stretch, two asymmetric deformations, one symmetric deformation, two rockings, and one torsion. . e computed (scaled) vibrations of the methyl groups, along with the experimentally observed frequencies and their corresponding assignments, are summarized in Table 2.

#### **UV-vis analysis**

UV–Vis spectrophotometry is essential for pharmaceutical analysis, as most drugs absorb light between 200 and 800 nm. . e Beer-Lambert law was applied to quantify BMBH by measuring its absorbance. Figure 3 presents the absorption spectra of BMBH, where its light absorption and transmission characteristics were initially determined experimentally using ethanol as a solvent. . e experimentally observed spectrum exhibited a maximum absorption wavelength ( $\lambda_{max}$ ) of 220.37 nm in ethanol with an absorbance value equal to 2.474.

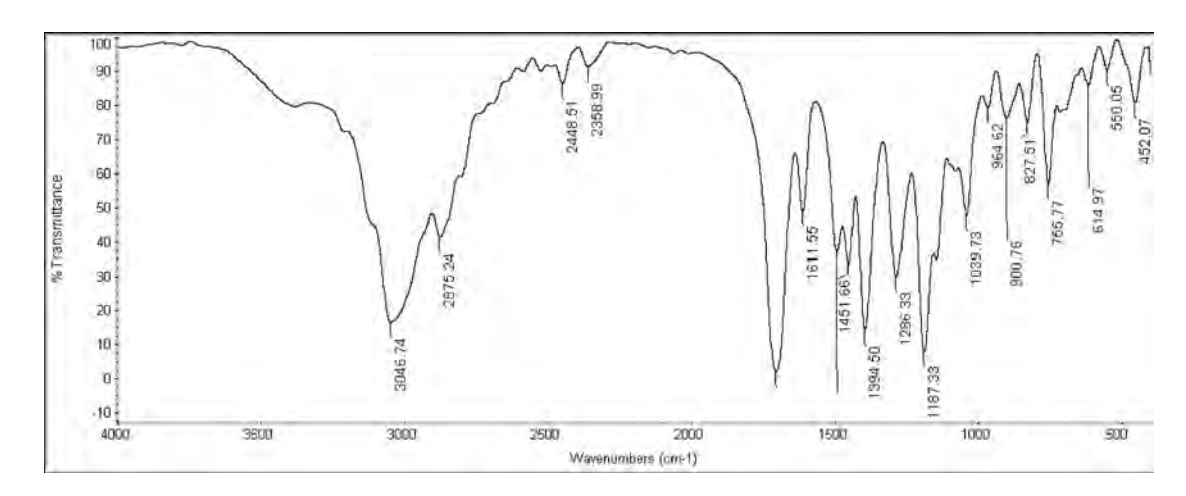


**Fig. 2.** Fourier transform infrared (FT-IR) spectrum of the BMBH structure, showing characteristic absorption bands corresponding to functional groups present in the material.

Assignment	Exp	intensity	Scaled	computed	NO
υ <sub>asy</sub> (CH3)	3002	37.36	3008	3134	1
v <sub>sy</sub> (CH3)	2898	119.99	2909	3031	2
S <sub>asy</sub> (CH3)	1446	88.65	1424	1484	3
S <sub>sy</sub> (CH3)	1359	105.86	1379	1437	4
ρasy(CH3)	1140	601.4	1136	1189	5
<sub>ρsy</sub> (CH3)	1002	62.61	1017	1064	6

**Table 2**. . e observed FT-IR and computed frequencies at RB3LYP /6–31 + G(d) level of DFT BMBH (methyl groups vibrations).  $\nu_{asy} \rightarrow$  asymmetric stretching.  $\nu_{sy} \rightarrow$  symmetric stretching.  $\nu_{sy} \rightarrow$  symmetric deformation.  $\nu_{sy} \rightarrow$  symmetric rocking.

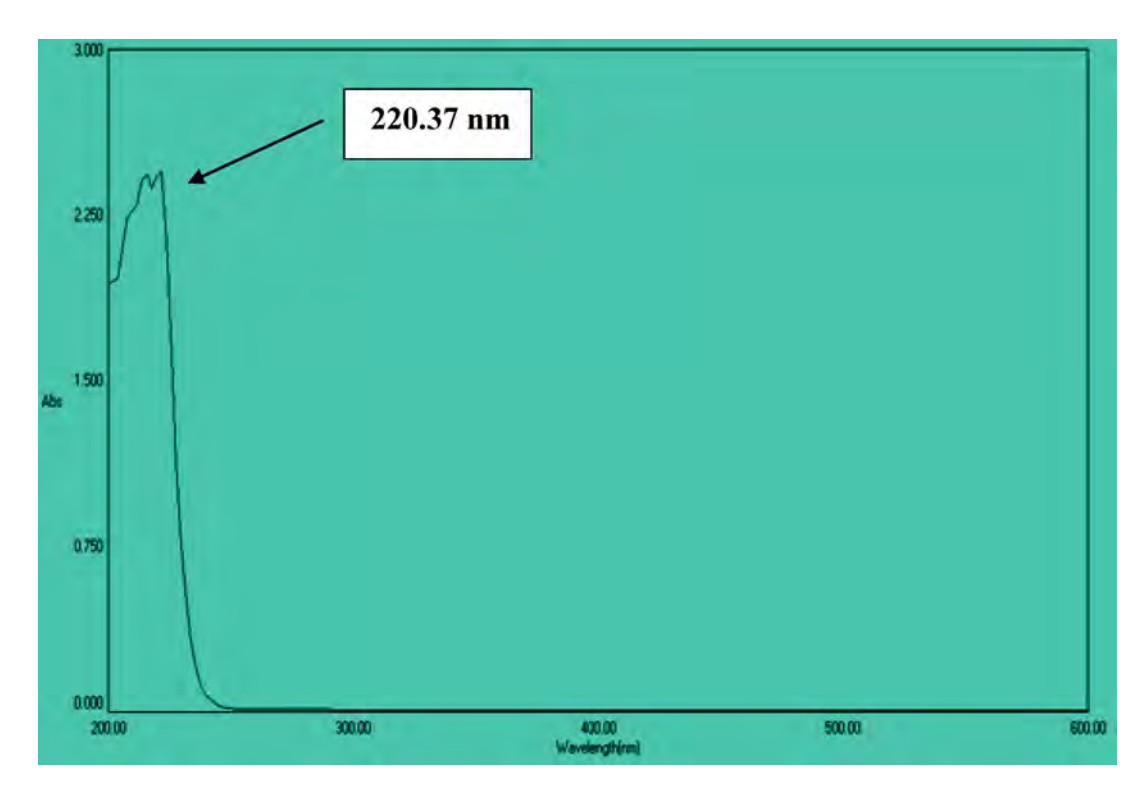


Fig. 3. UV-vis spectrum of BMBH, displaying the absorbance characteristics of the material.

#### XRD analysis

X-ray Di. raction (XRD) is used to analyze the crystalline structure of BMBH and detect any perturbations caused by physical, chemical, or environmental factors. Perturbations in XRD p atterns indicate changes in crystallinity, phase transitions, polymorphism, or interactions with excipients in pharmaceutical formulations. BMBH, in its crystalline form, exhibits sharp and well-defi ed di. raction peaks at characteristic  $2\theta$  angles, which correspond to its crystal lattice parameters. XRD analysis was used to show the synthesized complex's surface structural features and characteristics<sup>37</sup>. Figure 4 shows the results of observed peaks, where a sharp with high-intensity peak appears at  $2\theta$  of  $10^\circ$ . Th s high di. raction spectrum intensity refers to the studied compound's signifi ant crystallinity.

#### Computational studies

#### Geometry optimization

. e geometrically optimized parameters of BMBH computed by RB3LYP level with a 6-31+G (d) basis are listed in Table 3. . e corresponding structure and the labelling of atoms, is shown in Fig. 5. . e overall geometry has a non-planar structure. . e benzene ring's geometry is perturbed due to di. erent substituents on the benzene ring. . e symmetry of the ring is distorted, yielding ring angles greater than 120 at the points of substitution.

#### Mulliken and NBO analyses

Both Mulliken and NBO analyses help predict and rationalize experimental trends in spectroscopy and electrochemistry. . ey serve as preparatory tools for guiding experiments by predicting molecular properties, and validate experimental data by o. ering electronic structure explanations. . e charge distributions of the

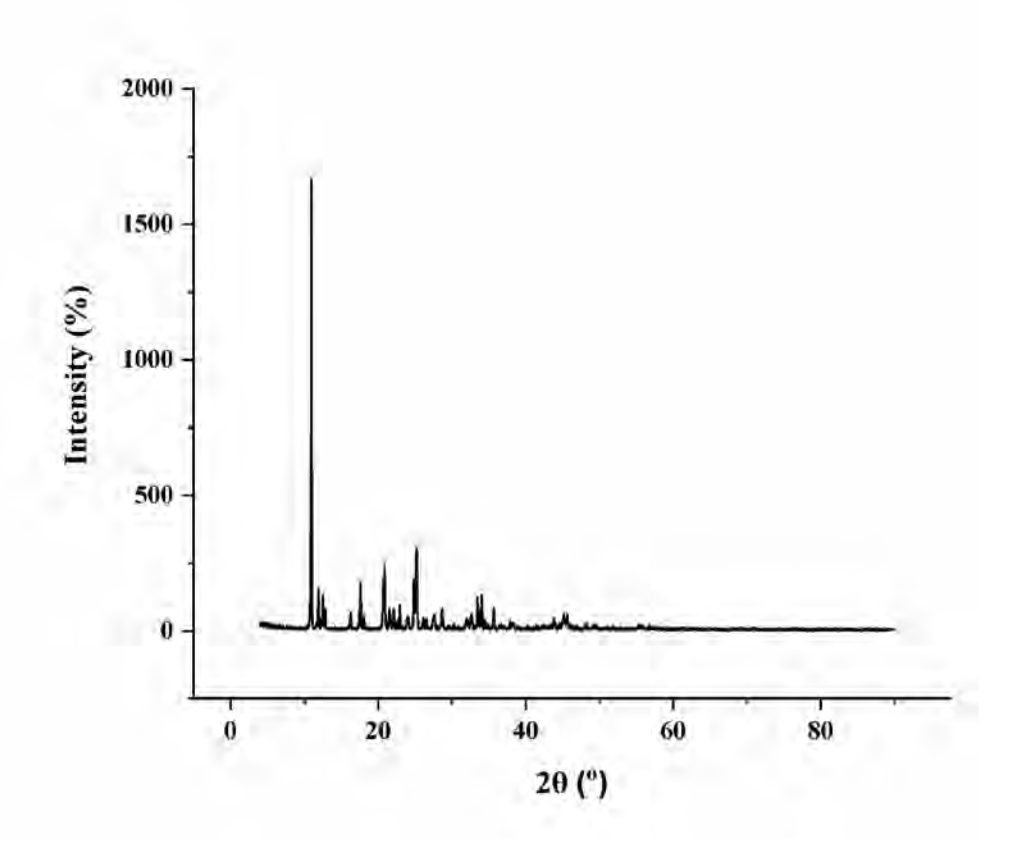


**Fig. 4**. e X-ray di. raction (XRD) spectrum of BMBH illustrates the crystalline structure through di. raction peak positions and intensities.

Bond lengths (A°)	Bond angles (°)	Dihedral angles (°)
O2-C18 1.39	O4-C21-N7 125.8	C21 O3 C22 O5 4.67
O4-C21 1.21	O2-C21-O4 123.39	C15C17 C18 O2 - 176.8
O3-C22 1.37	O3-C19-C20 116.3	C22O3 C19 C20 70.49
N7-C21 1.36	O2-C17-C18 116.8	C18 C20 C19 O3 – 176.19
N7-C23 1.46	C18-O2 -C21 118.5	C22 O3 C19 C15 52.55
N8-C22 1.36	C19-O3-C22 118.95	C25 N8 C22 O3 – 173.99
N6-C10 1.49	C21-N7-C24 124.17	C15C11C10 N6 - 165.11
Cl57- H42 1.87	C22-N7-C25 118.6	
Cl57-H32 3.19	O2-C20-C18 121.20	
	O5-C22-N8 125.6	
	C22N8-C26 124.2	

**Table 3**. Selected geometrical parameters of BMBH obtained by RB3LYP /6–31 + G(d) levels of DFT.

molecule have been computed by performing Mulliken analysis. . e theoretical calculations of atomic charges play an important role in the application of quantum mechanical calculations to molecular systems. . e calculated results have revealed the biggest values of the negative charge at O5, Cl57, and C9. . e carbon atoms of the methyl groups are positively charged. Almost very similar values of positive charges are noticed for all hydrogen atoms, forming  ${\rm CH_3}$  groups. . e highest value of the positive charge is located on H56, connected to N6 (N6-H56).

Natural bond orbital analysis of BMBH is done with NBO 3.1 in Ga ussian 09 to confi m charge transfer and conjugation. A second-order perturbation approach, the Fock matrix gives an examination of the energetic importance of electron transfer from the donor (Lewis-type NBOs) to the acceptor (non-Lewis NBOs). . e stabilization.

energy,  $E_{(2)}$ , represents the degree of electron transfer from donor to acceptor and is known as the degree of electron delocalization<sup>38</sup>.

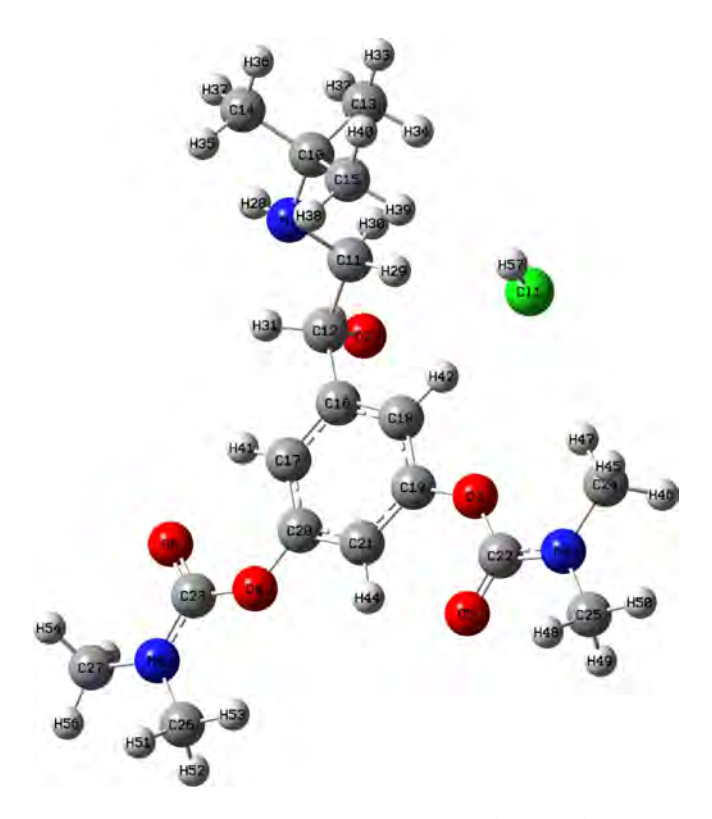


Fig. 5. Optimized structures with numbering of atoms of BMBH.

F (i,j) a.u	Ej-Ei a.u	E (2) kcal/mol	Acceptor j	Donor i	
0.059	0.37	10.71	π* C16-C19	LP (2)O3	(1)
0.130	0.58	35.92	σ* O2-C21	LP (2)O4	(2)
0.117	0.72	22.60	σ* N7- C21	LP (2)O4	(3)
0.130	0.58	35.62	σ* O3- C22	LP (2)O5	(4)
0.117	0.72	22.60	σ* N8- C22	LP (2)O5	(5)
0.113	0.35	45.57	σ* O4- C21	LP (1)N7	(6)
0.112	0.36	43.99	σ* O5- C22	LP (1)N8	(7)
0.190	0.36	102.55	LP* H27	LP (4) Cl57	(8)
0.082	0.01	220.31	C15-C17	BD (2) *C18-C20	(9)
0.082	0.01	231.09	C15-C17	BD (2) *C16-C19	(10)

Table 4. Second-order perturbation analysis of the Fock matrix of BMBH.

$$E_{(2)} = \Delta E_{i j} = q_{i j} = \frac{F(i, j)^2}{Ej - Ei}$$
 (1)

where  $q_{ij}$  is donor orbital occupancy, F (i, j) is the off-d agonal Fock matrix element, and  $E_j$  and  $E_i$  are the diagonal elements (orbital energies). . . e  $E^{(2)}$  value can represent (refl. ct) the intensity of the electron donor and electron acceptor and the degree of conjugation of the structure. Table 4 displays the predicted intensities between the donor and acceptor NBOs, from which we can observe the interaction orbitals and their interaction intensities. Intramolecular interactions arise from  $\pi(C-C) \rightarrow \pi^*(C-C)$  overlap and  $LP \rightarrow \sigma^*(O-C)$  and (N-C) transfer. . ese contribute to charge transfer and hydrogen bonding, making the main contribution to the stabilization of the system.

A signifi ant contribution to the stabilization energy could be added by LP Cl57  $\longrightarrow$  LP\* H27 at a value of 102.55 in E  $^{(2)}$  (Table 4).

#### Frontier molecular orbitals (FMOs)

Frontier Molecular Orbital analysis is a powerful theoretical tool that enhances the interpretation of experimental data in various fi lds of chemistry, materials science, and biochemistry. e highest occupied molecular orbital (HOMO) and the lowest unoccupied molecular orbital (LUMO) energies, along with their gap, provide

fundamental insights into electronic transitions, chemical reactivity, and molecular stability. HOMO and LUMO energies of the title compound were computed with the same level of DFT theory and are shown pictorially in Fig. 6. . e compositions of both HOMO and LUMO were calculated by the Becke method via the Multiwfn program. From Fig. 7, it can be seen that the HOMO result from the lone pair present on the chloride atom contributes to the HOMO by 96.7%. . e LUMO results mainly from the aromatic system (benzene ring), with a contribution of 78%. . e chemical reactivity of the title compound would be assessed based on the global reactivity descriptors. . e energy of the HOMO and LUMO is directly related to the ionization potential (IP) and electron affi ty (EA).

. e value of IP and EA are given according to Koopman's theorem<sup>39</sup>.

$$IP = -HOMO (2)$$

$$EA = -LUMO (3)$$

. e values of IP and EA can be used to deduce the global reactivity descriptors, including chemical potential  $(\mu)$ , chemical hardness  $(\eta)$ , chemical so. ness(S), electronegativity (X), and electrophilic index  $(\omega)$  according to the following equations.

$$\mu = -\left[ \left( IP + EA \right) / 2 \right] \tag{4}$$

$$\eta = (IP - EA)/2 \tag{5}$$

$$S = 1/2\eta \tag{6}$$

$$X = (IP + EA)/2 \tag{7}$$

$$\omega = \mu^2 / 2\eta \tag{8}$$

According to the values in Table 5, (E)/ (N max) is -1.707eV, and the maximal charge acceptance Nmax is 1.203eV. . ese values reveal the drug's intramolecular charge transfer as well as its ability to interact with and bind to  $\beta 1$ -adrenergic receptors.

. e chemical hardness  $(\eta)$  and the electron transfer energy (E) are 2.836 and -2.055 eV, respectively. . ese fi dings suggest that the charge transfer process in the drug and bioactivity formation of intermolecular interaction with 1-adrenergic receptors and blocking is permissible<sup>40</sup>. Relative to biological impact, a higher

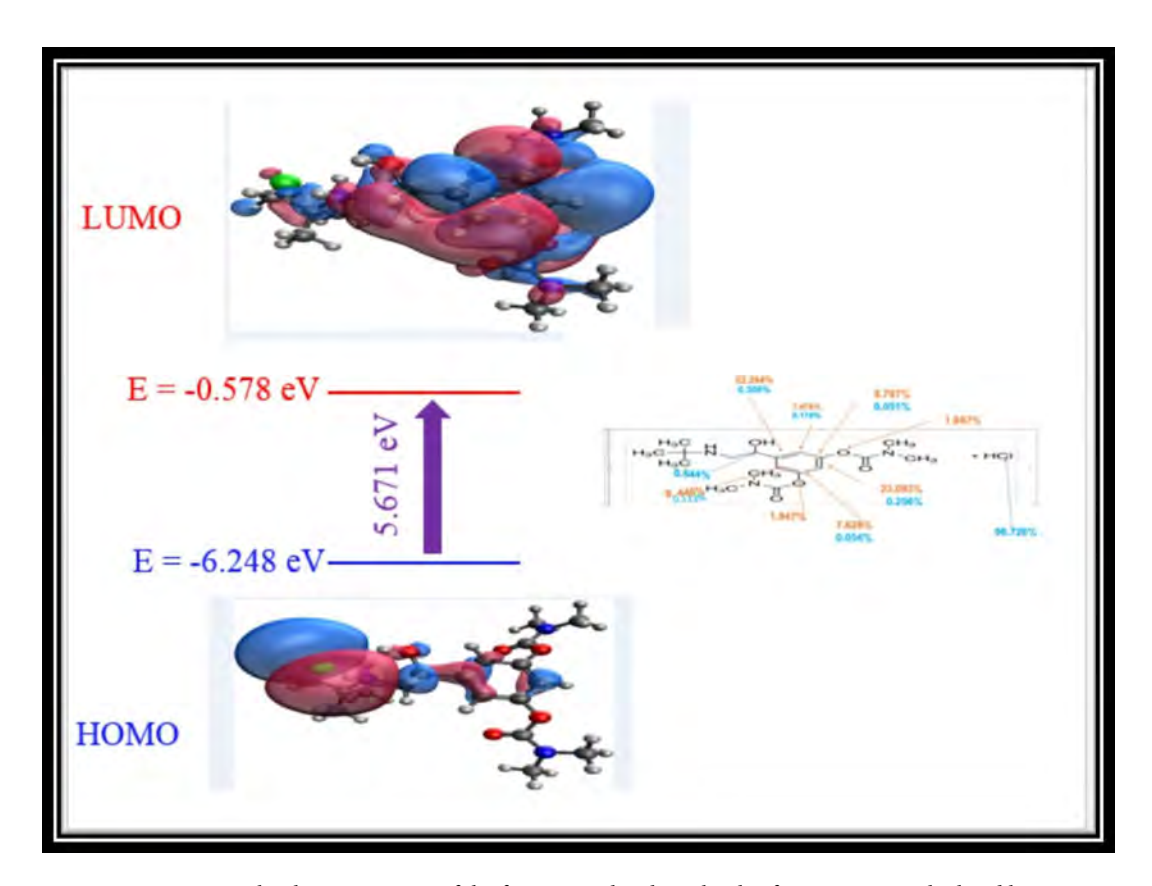


**Fig. 6.** . e atomic orbital compositions of the frontier molecular orbitals of BMBH were calculated by the Becke method. Percentage contributions to the HOMO and LUMO are given in blue and red colors respectively.

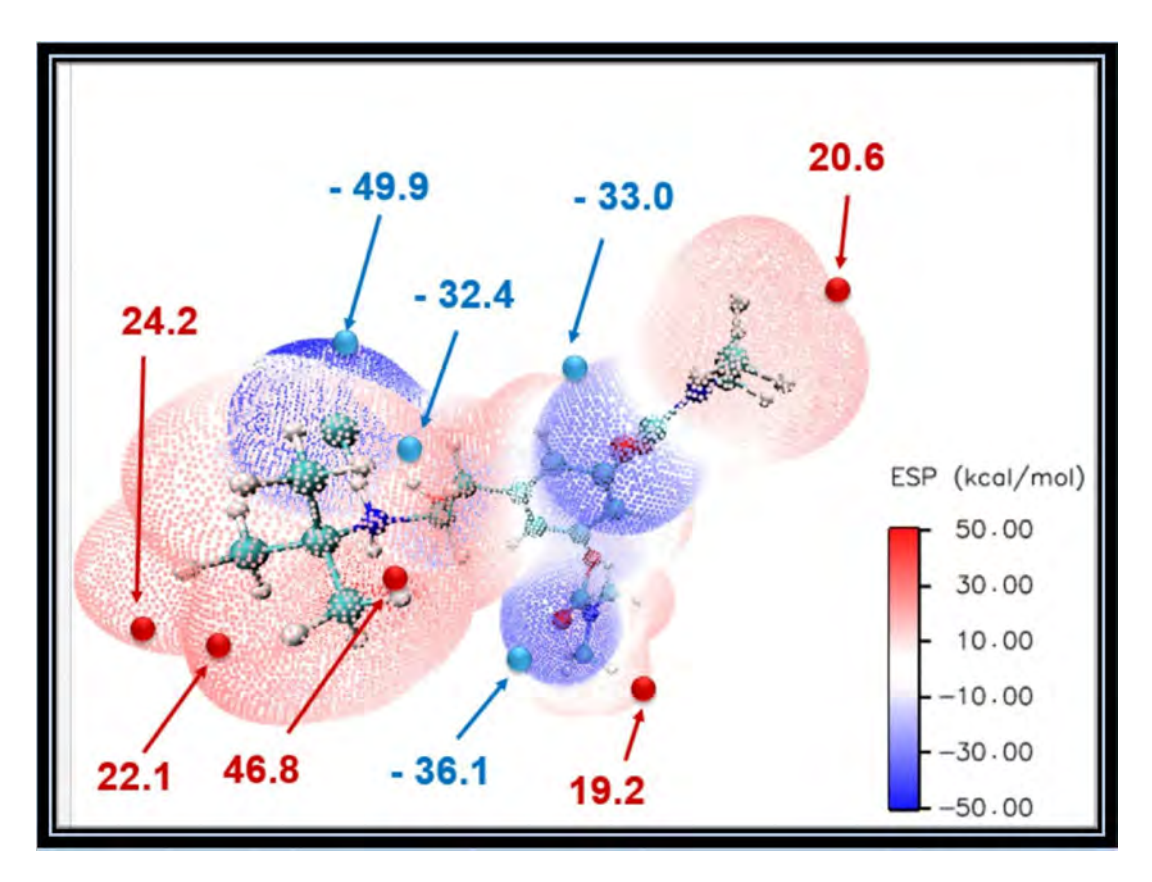


Fig. 7. 3D molecular electrostatic potential map for BMBH along with the values of its electrostatic and vdW surfaces with colored scale potential values.

Chemical reactivity descriptor	Value
Ionization potential (I)	6.248 eV
Electron affi ty (A)	0.578 eV
Electronegativity (χ)	3.414 eV
Chemical potential (µ)	- 3.414V
Chemical hardness (η)	2.836 eV
Chemical so. ness (S)	0.352 eV
Electrophilicity index (ω)	2.055 eV
Energy change ( $\Delta E$ )	-2.055 eV
Maximal charge acceptance ( $\Delta N_{ma}$ )	1.203 eV
$\Delta E/\Delta_{max}$	-1.707 eV

**Table 5**. Activity parameters of BMBH, including key chemical reactivity descriptors.

HOMO–LUMO gap (5.671 eV) and higher  $\omega$  (2.055 eV) predicted the interaction of the designed structure with nucleophilic sites in DNA (e.g., guanine N7) or protein functional groups (–SH, –NH<sub>2</sub>). Additionally, BMBH has more negative HOMO energy (–6.248 eV), it may act as an electron acceptor, potentially forming hydrogen bonds or covalent interactions with biomolecules. . ese properties can in uence binding affi ty, biodegradation, and toxicity, which are important for drug design or toxicity assessment<sup>41,42</sup>.

### . e molecular electrostatic potential (MEP) map

To predict reactivity, MEP identifies nucleophilic and electrophilic sites, also it analyzes biological recognition and hydrogen bonding. One can use the concept of molecular electrostatic potential (MEP), which is connected to electron density<sup>43</sup>. Drug-receptor interactions and the electrostatic potential (ESP) V(r) have both been extensively studied<sup>44,45</sup>. e 3D ESP map shows potential values at electrophilic and nucleophilic sites. e most electrostatically positive, most negatively charged, and zero electrostatic potential regions are represented by the colors blue, red, and white on the MEP surface, respectively. Figure 7 shows surface maxima for positive potential sites surrounding the hydrogen atoms and 4 surface minima for the negative potential sites on chlorine

and oxygen atoms. e global minimum on the surface (-49.9 kcal/mol) is located on Cl57. While the location of the surface's global maxima (+46.8 kcal/mol) is located on H27, we note that the strongest nucleophilic and electrophilic sites, as well as the global maximum and minimum, are found in the vicinity of hydrogen chloride. e MEP map shows that the hydrogen chloride region is highly biologically active and crucial for drug recognition.

#### Density of states (TDOS and PDOS)

TDOS and PDOS are essential computational tools that help explain and predict experimental results across spectroscopy, solid-state physics, and electrochemistry. . eir theoretical insights bridge the gap between quantum calculations and real-world materials behavior, aiding in material design and technological advancements.

. e Partial Density of States (PDOS) of BMBH is a crucial property in computational material science and quantum chemistry. It describes the contribution of specific atomic orbitals or elements to the total electronic Density of States (DOS). It provides insights into the molecule's electronic structure, bonding characteristics, and reactivity<sup>46</sup>.

BMBH, a prodrug of terbutaline, consists of a complex molecular structure containing elements such as carbon (C), hydrogen (H), oxygen (O), nitrogen (N), and chlorine (Cl). By calculating the PDOS using Density Functional . eory (DFT) methods, we can analyze how di. erent atomic orbitals contribute to the electronic states near the Fermi level. . e structure was classifi d into fragments, where each part could export the main contributed levels to form the structure identity. From Fig. 8, it was observed that Fragments 8, 5, and 1 can contribute the most contribution of the electronic levels in leading to the structure stability. However, fragment

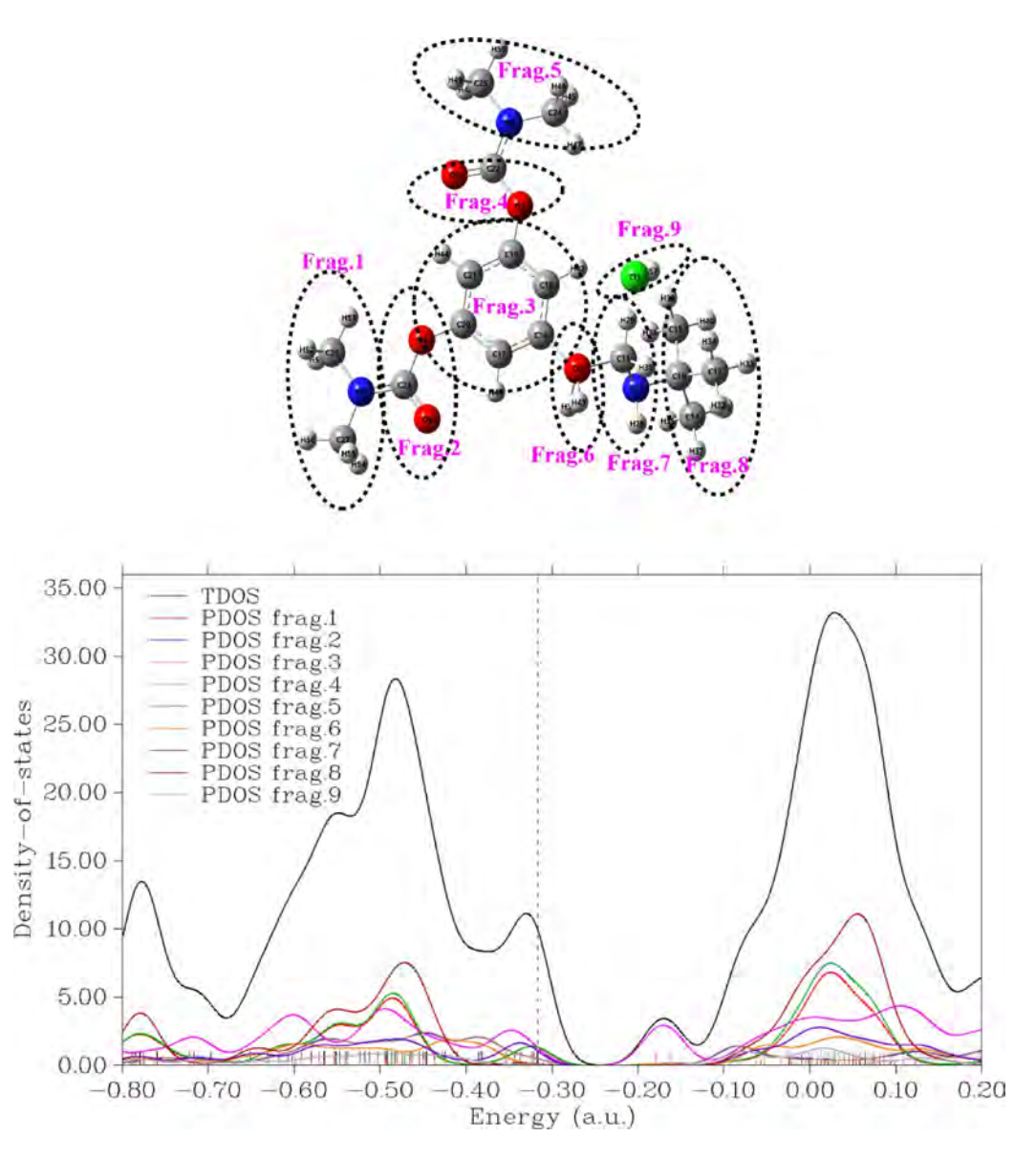


**Fig. 8**. Total density of states (TDOS) and partial density of states (PDOS) for fragments of BMBH, illustrating the electronic structure and contribution of di. erent molecular orbitals.

9 (HCl) shares with minimum orbital contribution, concluding its interaction with a weak H-bonding nature inside the molecule.

#### Reduced density gradient (RDG) analysis

RDG provides a deeper understanding of noncovalent interactions, guiding the interpretation of experimental results and assisting in the design of new materials, drugs, and catalysts. Equation 9 gives the reduced density gradient (RDG), which is a fundamental dimensionless quantity derived from the density and its fi st derivative<sup>47</sup>.

$$RDG(r) = \frac{1}{2(3\pi^2)^{\frac{1}{3}}} \frac{\nabla \rho(r)}{\rho(r)^{\frac{4}{3}}}$$
(9)

Large negative values of sign ( $\lambda_2$ ) in RDG tails indicate attractive interactions (such as dipole–dipole or hydrogen bonding); if the sign ( $\lambda_2$ ) is large and positive, the interaction is non-bonding (steric e. ect).

In Fig. 9, green colors are identified as van der Waals interactions, while the red color is identified as strong repulsion. Repulsive interactions were observed inside the ring, while van der Waals interactions were observed between the hydrogen atoms. . e negative value of the sign  $(\lambda_2)$  shows the weak hydrogen bonding interactions  $^{48,49}$ .

#### Electron localization function (ELF)

- . e Electron Localization Function (ELF) s erves as a valuable tool for analyzing the electronic structure, bonding nature, and atomic shell distribution across the molecular surface. e electron distribution within the compound is analyzed and interpreted using the Electron Localization Function (ELF) and Localized Orbital Locator (LOL). e fundamental principle governing ELF is Pauli repulsion, which arises due to an excess of kinetic energy density. Regions where opposite spin-paired electrons or single electrons exhibit maximal localization are characterized by an ELF value approaching 1, indicating areas of maximum Pauli repulsion. Conversely, regions with minimal electron localization correspond to ELF values near 0. Due to Pauli exclusion forces, highly localized electron regions delineate atomic shells, chemical bonds, and lone pair electrons, e. ectively explaining the most repelled electronic domains 50.
- . e ELF contour map, generated using Multiwfn so. ware and displayed in Fig. 10a, highlights regions of varying electron density. High ELF values (0.85–1.0 B ohr) signify strong electron localization, indicative of covalent bonding, whereas low ELF values (0.0–0.4 Bohr) refl ct pronounced electron delocalization. . e ELF visualization further reveals intense electron concentration around hydrogen atoms, depicted in red, while delocalized electron regions surrounding oxygen and carbon atoms appear in blue. Notably, strong electron localization is observed between carbon atoms within the ring and bonded hydrogen atoms, resulting from the overlap between the carbon sp orbitals and hydrogen s orbitals. Additionally, the perturbation in ELF distribution near oxygen atoms is attributed to interactions involving hydrogen and halogen bonds.
- e three-dimensional (3D) ELF plot for BMBH is presented in Fig. 10b. In this representation, monosynaptic basins correspond to lone electron pairs, whereas disynaptic basins are indicative of covalent interactions. Monosynaptic regions of oxygen, nitrogen, and chlorine are widely distributed. Disynaptic basins of OH, NH, and CH bonds are more confi ed due to hydrogen and halogen bonding.

#### AIM calculations

. e atoms in molecules (AIM) theory are a convenient method to analyze the hydrogen bonding and other interactions in various molecular systems. It has been extensively used to classify and understand bonding interactions in terms of quantum mechanical parameters and their derivatives as electron density ( $\rho$ ). . e theory of AIM has efficiently described the H-bonding, and it's a concept without borders. One of the advantages of this theory is that one can obtain information on the change in electron density distribution as a result of their bond formation or complex formation<sup>51</sup>. . e molecular graph of the molecule using AIM theory is shown in Fig. 11. . e topological parameters of non-covalent interactions are grouped in Table 6. . e AIM results show that BMBH is characterized by 4BCPs of non-covalent character. Two describe hydrogen bonding, and two characters halogen bonding interactions. According to the values of the parameters reported in Table 5. We can classify the non-covalent interactions as weak hydrogen and halogen bonding interactions, except for N6-H27......Cl57 strong bonding interactions<sup>52</sup> (Table 6; Fig. 11).

#### Nonlinear optical (NLO) e. ects

. e nonlinear optical (NLO) e. ects arise from the interaction of electromagnetic fi lds. It is applied in various media to produce new fi lds altered in phase, frequency, amplitude, optical switching, optical logic, and other propagation characteristics from the incident fi lds. . e molecules with NLO properties have been extensively investigated due to their applications in t he areas of signal processing, telecommunication, and optical interconnection. . e calculations of the total molecular dipole moment ( $\mu$ ), mean linear polarizability ( $\alpha$ ), and mean fi st hyperpolarizability ( $\alpha$ ) from the Gaussian output have been explained in detail previously<sup>53</sup>. . ese parameters help in optimizing the molecular modifi ations of the studied structure, aiming to improve the pharmacological e. ects.

Table 7 shows the dipole moment, polarizability, and fi st hyperpolarizability components of the drug compound, whose invariant is calculated with a numerical derivative of the dipole moment using the RB3LYP/6–31+G(d) level of DFT. . e total static dipole moment, average linear polarizability, anisotropy of polarizability, and fi st hyperpolarizability were calculated according to the reference<sup>54</sup>.

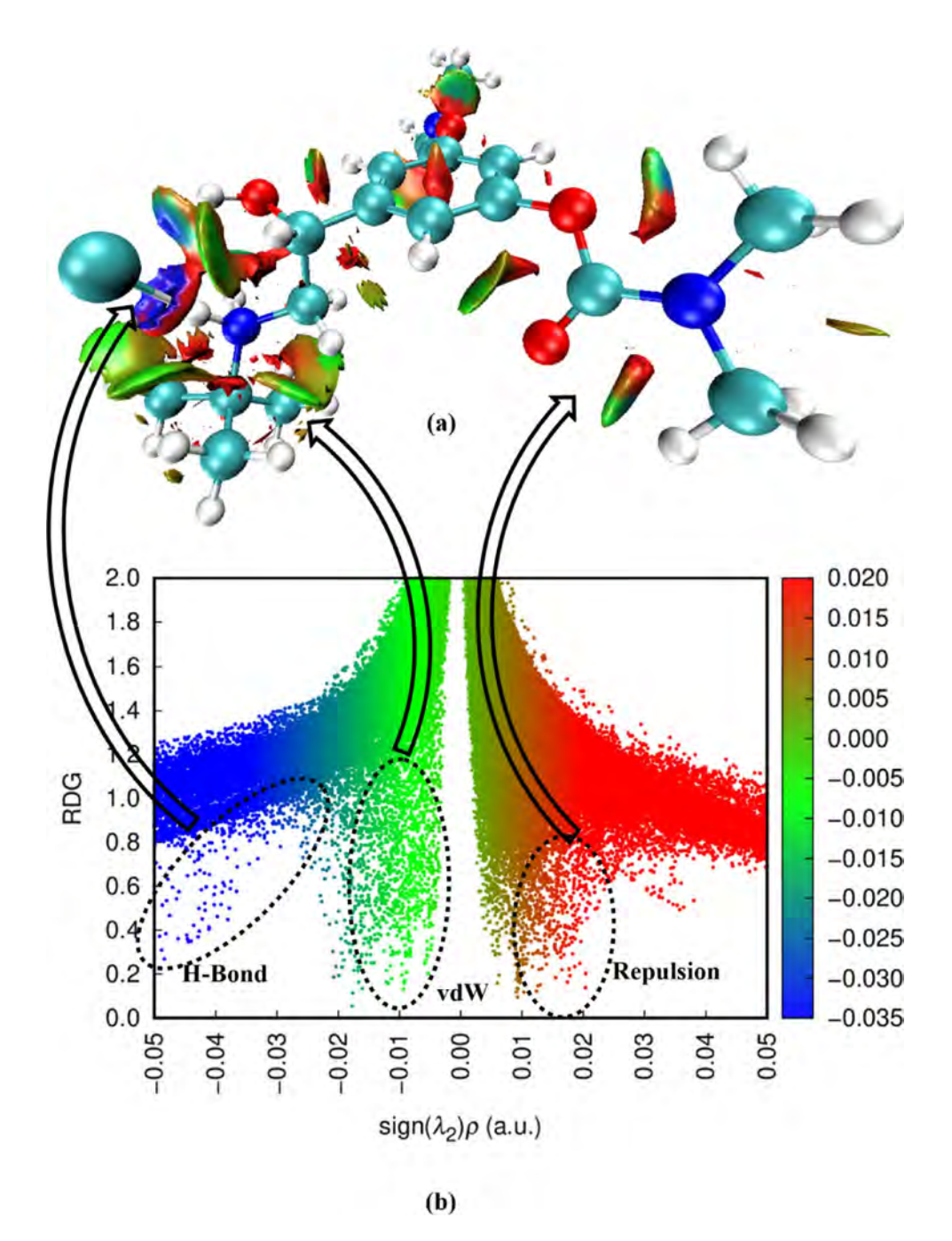
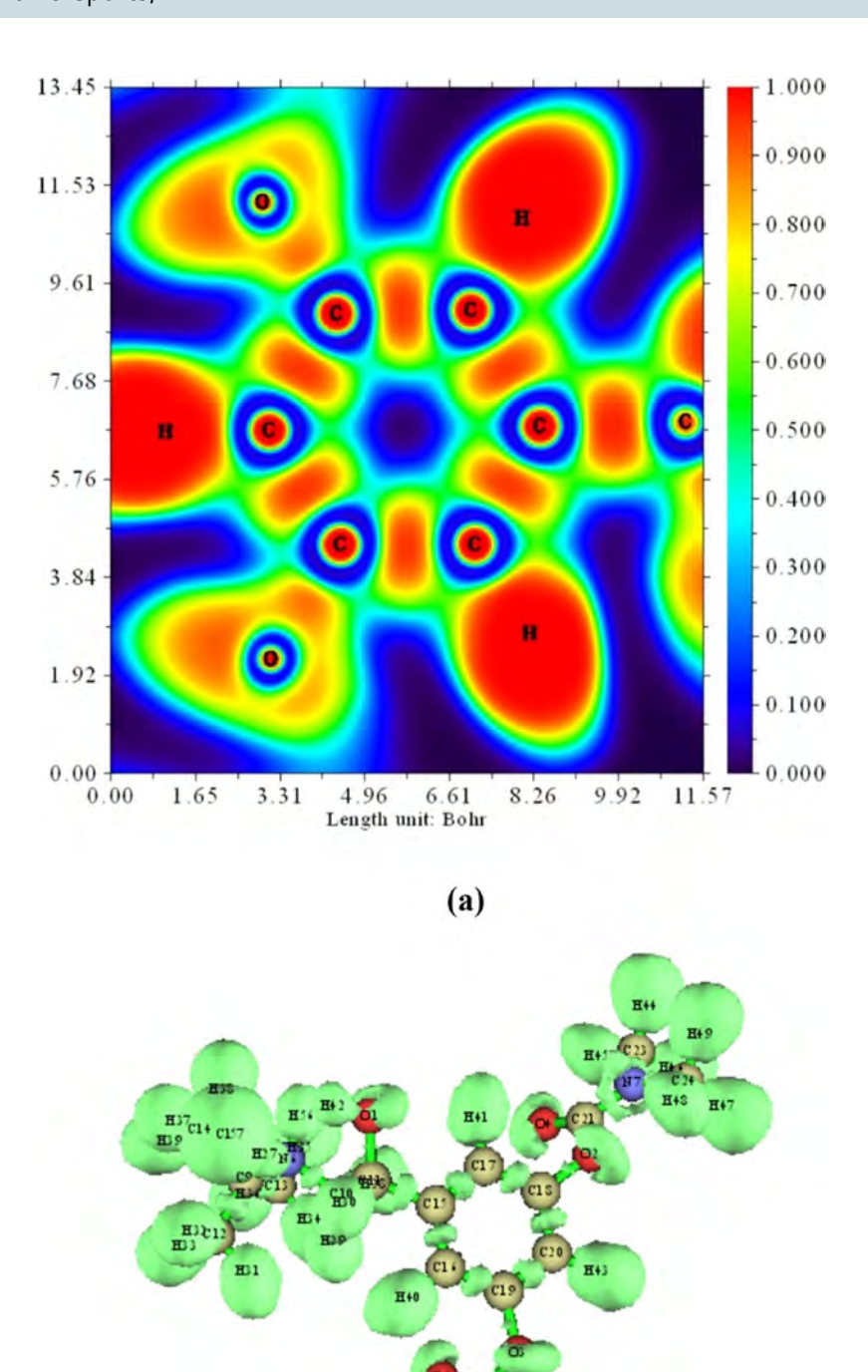


Fig. 9. (a) RDG map versus the electron density ( $\rho$ ) multiplied by the sign  $\lambda_2$  for BMBH (b) . e surfaces are colored on a blue-green–red scale according to values of sign  $\lambda_2$ .

. e calculated values of total static dipole moment  $\mu$ , the average linear polarizability  $\alpha$ , the anisotropy of the polarizability  $\Delta\alpha$ , and the fi st hyperpolarizability  $\beta$  using the RB3LYP/6–31+G(d) level of the DFT method are 8.5 Debye, 297.5 a.u., 540.42 a.u., and  $2.676\times10^{-30}$  e.s.u.

Urea is one of the prototypical molecules used in the study of the NLO properties of molecular systems, and it is frequently used as a threshold value for comparative purposes. . e values of  $\mu,\alpha$ , and  $\beta$  obtained with the RB3LYP/6–31+G(d) method for urea is 1.373 Debye, 3.831 Å3, and 3.729  $\times$  10<sup>-31</sup> cm $^5$  e.s.u. $^{-1}$ , respectively  $^{55}$ . e drug compound's fi st- and second-order polarizabilities are greater than those of the urea. . e title compound may be a potential candidate in the development of NLO materials based on the magnitude of its fi st hyperpolarizability. As a result, this molecule could serve as a potential building block for nonlinear optical materials.



**Fig. 10**. (a) Electron localization function (ELF) color map, and (b) 3D plots ELF-isosurfaces, for BMBH with depicting the electron density distribution and localization in the molecular structure.

(b)

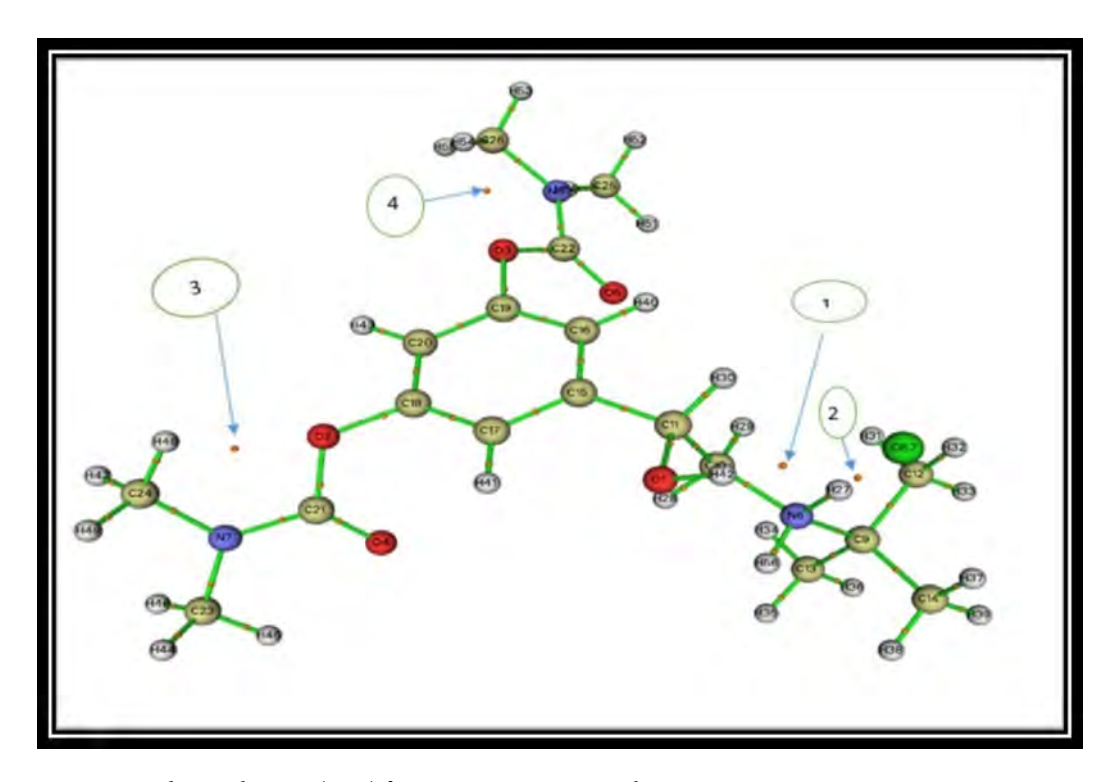


Fig. 11. Bond critical points (BCP) for BMBH using AIM analysis.

E <sub>bond</sub> kJ/mol	ELF (a.u)	V (r) a.u Localization potential	$ abla^2  ho(r)$ a.u Laplacian of the electron density	ρ(r) a.u Electron density	Interactions
-19.7	0.08778	-0.01506	0.061778	0.001682	O1-H42CL57
- 57.95	0.30722	-0.044249	0.10121	-0.009472	N6-H27CL57
-18.73	0.03816	-0.014301	0.08193	0.003090	C21-O2H48
-18.36	0.038257	-0.01402	0.082101	0.003095	C26-H54O3

**Table 6**. Topological parameters of the non-covalent interactions of BMBH.

Values	Components	Values	Components
246.283	$\beta_{xxx}$	5.81840	$\mu_x$
- 303.285	$\beta_{xyy}$	-1.48979	$\mu_y$
-3.73170	$\beta_{xzz}$	-6.12364	zμ
-146.087	$\beta_{yyy}$	308.136	α <sub>xx</sub>
-26.1894	$\beta_{xxy}$	307.742	α ,,,
-142.729	$\beta_{yzz}$	222.910	$\alpha_{zz}$
-62.19	$\beta_{zzz}$	4.89543	α <sub>xy</sub>
28.1994	$\beta_{xxz}$	1.15448	α <sub>xz</sub>

**Table 7**. Calculated dipolemoment  $\mu$  (Debye), polarizability( $\alpha$ ) and thefi st hyperpolarizability ( $\beta$ ) components(a.u.) of BMBH.

#### Simulation of molecular dynamics for BMBH interacting with a graphene surface

MD simulation in solid state adsorption systems can support the stability of the designed models and increase the prediction of drug transport in pharmaceutical approaches. . e designed BMBH/Graphene system was studied via the noncovalent interaction computational method GGA/PBE related to the DFT category. . e Forcite module was utilized with ensemble NVT to describe the energy and temperature changes through the simulation time of 1000 ps. . e dynamic analysis estimates values of potential energy ( $E_{\rm pot}$ ) and kinetic energy ( $E_{\rm kin}$ ) for each simulation step before and a. er adsorption. Figure 12a,b illustrate the energy parameter changes for the separated BMBH and graphene system compared with their adsorption system. As shown, the energetic variables are low with BMBH drug, while the other species exported larger energetic simulations with both

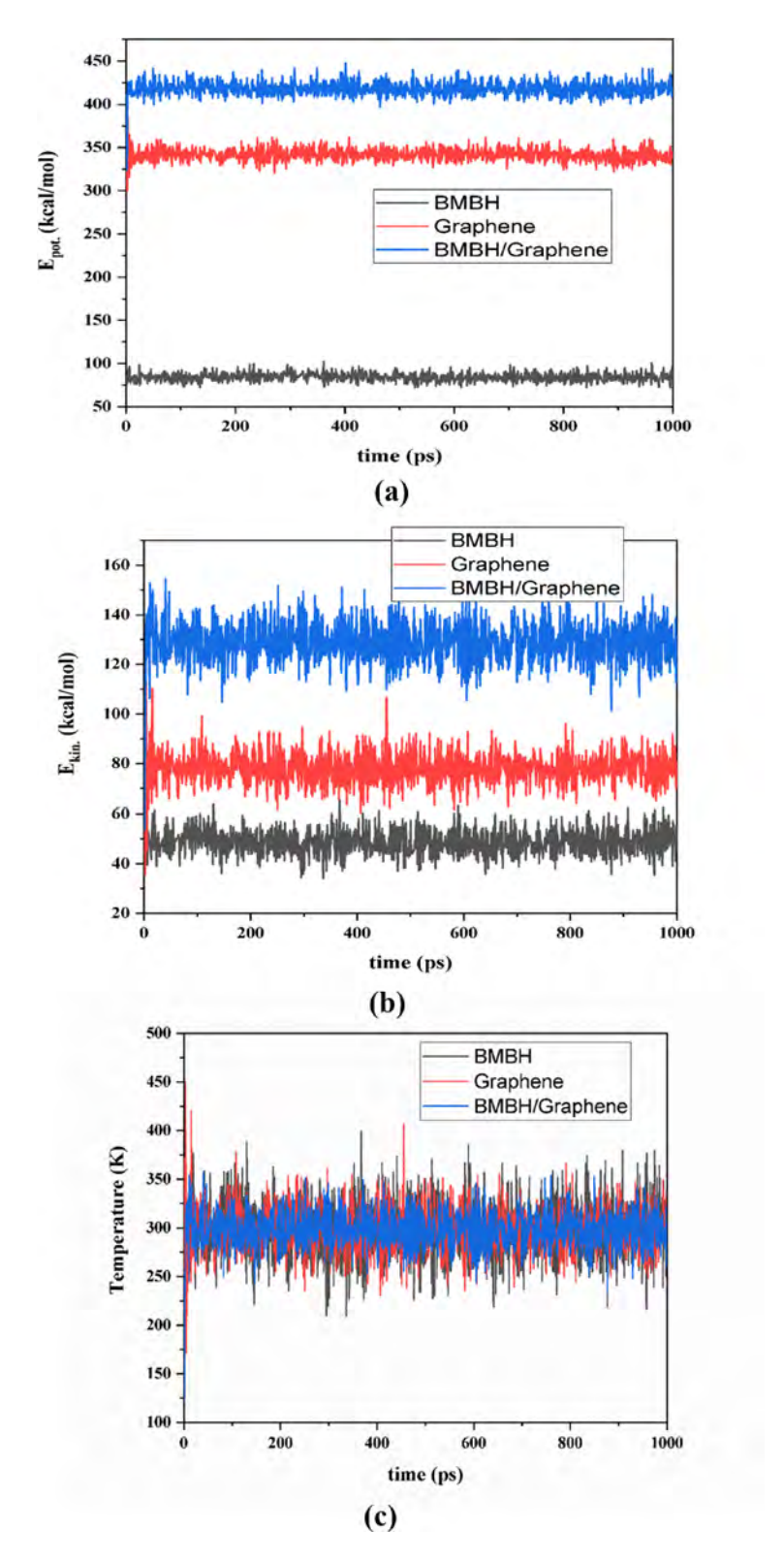


Fig. 12. (a) potential energy variable, (b) kinetic energy variable for the designed systems before and a. er adsorption during dynamic simulation, and (c) temperature change through simulation time for un adsorbed and adsorbed systems.

 $\rm E_{pot}$  and  $\rm E_{kin}$ . However, the potential energy curves in the exported signifi antly higher values with the BMBH/graphene adsorption system. Figure 12c shows the changes in temperature for each system, and this shows less floculated values with the BMBH/graphene adsorption system, while all designed curves dynamically moved around 300 K... e results predicted some stability in the adsorption formed system, which may be motivated by the drug delivery approach.

#### BMBH/graphene adsorption energy estimation

To predict the noncovalent interactions, present on the surface of Graphene via the adsorption of BMBH, GGA/PBE geometric optimization was followed by an examination of the adsorption location. . e adsorption locator module predicted the preferred adsorption mechanistic models, in which the fi st model was arranged to be more stable, to confi m the occurrence of some interactions in the adsorption mechanism. . e di. erence between a species' energies before and a. er adsorption can be used to anticipate the system's calculated adsorption energy<sup>56–58</sup>.

$$E_{ads} = E_{\text{BMBH/Graphene}} - \left( E_{\text{BMBH}} + E_{Graphene} \right) \tag{10}$$

where  $E_{\rm BMBH}$  is the energy of the adsorbate,  $E_{\rm Graphene}$  is the energy of the adsorbent surface and  $E_{\rm BMBH/Graphene}$  is the overall energy of the adsorption system. . e interaction of BMBH on the graphene surface can be controlled with hydrogen atoms interacting with the  $\pi$ -electronic mobility of the graphene phenyl ring. Also, other intramolecular close contacts between Cl and H of the CH $_3$  group can support the system's stability. This adsorption study may be helpful in several applications such as drug delivery and excess drug removal in medical and pharmaceutical strategies. As illustrated in Fig. 13, two best-proposed interaction models exhibit close-contact non-covalent interactions, which are primarily ranged from 10 designed models for BMBH/Graphene adsorption system. . e adsorption behavior is characterized by the energetic parameter values. . e adsorption energy values resulting from surface interactions exported the order from 1 to 10 as shown in Fig. 14, where models number 1 and 3 estimated the optimum binding affity (-31.22 kcal/mol and -30.93 kcal/mol, respectively). . e predicted adsorption study may give an important insight into system stability aiming to hydrogen storage on the electronic-rich surface. . e noncovalent interactions present on the surface can be summarized as the adsorption stability of BMBH on Graphene is governed by  $\pi$ - $\pi$  stacking, electrostatic interactions, hydrogen bonding, and charge transfer e. ects. . e moderate binding energy suggests its potential for reversible adsorption, making it useful for drug delivery and hydrogen storage applications.

Structures	Total energy	Adsorption energy	Rigid adsorption energy	Deformation energy	compound : dEad/dNi
3D Atomistic-1	4.764215	- 198.539	-31.2231	- 167.315	-198.539
3D Atomistic-2	5.027971	- 198.275	-30.8372	-167.438	-198.275
3D Atomistic-3	5.682667	- 197.62	-30.9342	-166.686	-197.62

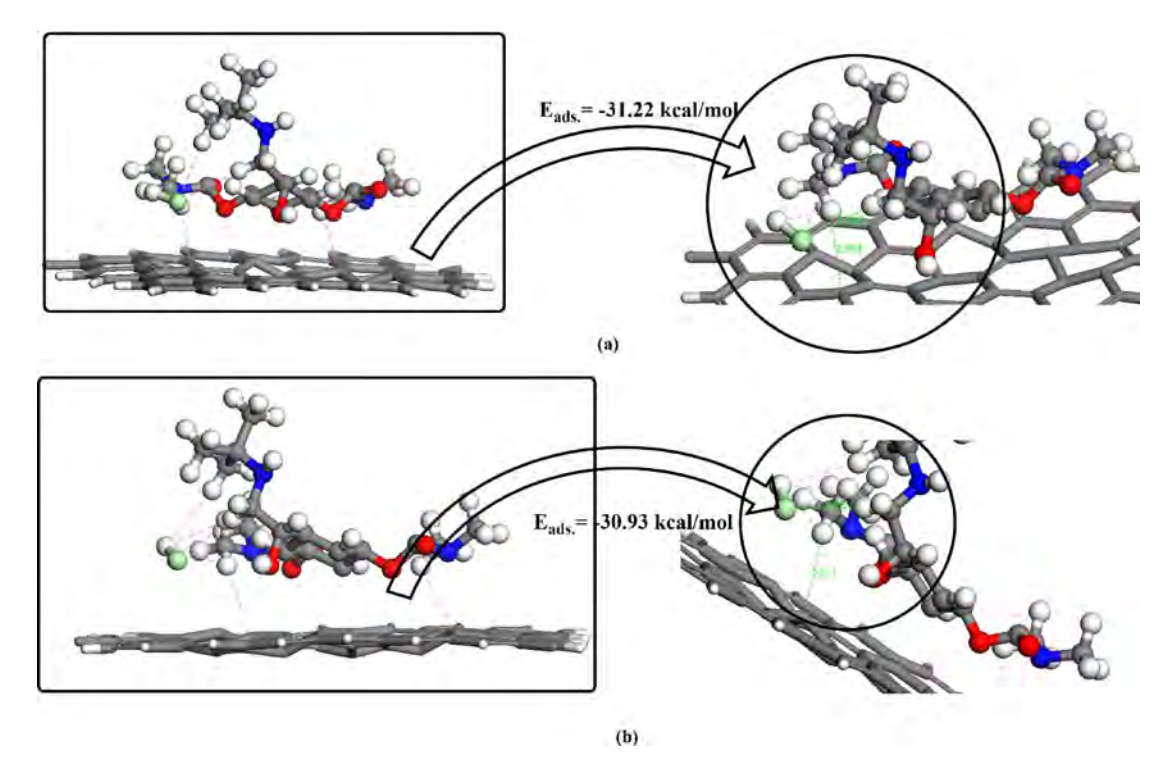
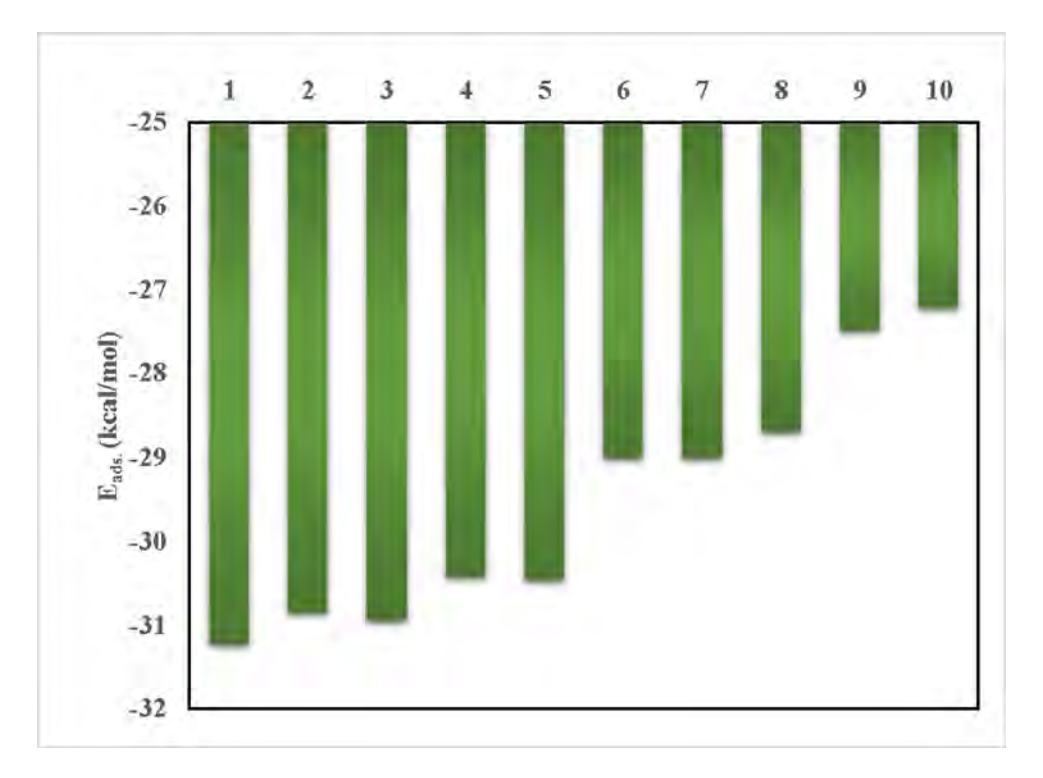


Fig. 13. e best BMBH/graphene adsorption models using the adsorption locator module.



**Fig. 14**. Correlation between the adsorption energy parameter and the interaction system type across 10 generated models for BMBH/graphene adsorption system.

Structures	Total energy	Adsorption energy	Rigid adsorption energy	Deformation energy	compound : dEad/dNi
3D Atomistic-4	5.916225	- 197.386	-30.4179	- 166.969	-197.386
3D Atomistic-5	6.542835	- 196.76	-30.4465	-166.313	-196.76
3D Atomistic-6	6.795467	- 196.507	-28.9929	- 167.514	-196.507
3D Atomistic-7	7.077594	- 196.225	- 28.9945	- 167.231	-196.225
3D Atomistic-8	7.609889	- 195.693	-28.6793	-167.014	-195.693
3D Atomistic-9	7.97483	- 195.328	-27.4851	- 167.843	-195.328
3D Atomistic-10	8.193138	- 195.11	-27.2049	- 167.905	-195.11

#### Molecular docking analysis

Docking protocol was validated by re-docking of the co-crystalized thio. avine T at the active site of butyrylcholinesterase (PDB ID: 6ESY), Fig. 15A. the re-docking rmsd = 1.16 Å and binding score = -5.75 kcal/mol. All the key interactions accomplished by the co-crystalized ligand with the key amino acids in the binding site are reproducible using the docking setup, mentioned in the experimental section. e validated docking setup was then used to investigate the ligand-receptor interactions and binding patterns for bambuterol hydrochloride (score = -7.99 kcal/mol), Fig. 15B. e amino acid residues involved in interaction at binding site with co-crystallized thio. avine T are.

Asp70, Trp82, Tyr332, where the main interactions are ionic and  $\pi$ -cation with amino acid residues Asp70 and Tyr332 and  $\pi$ - $\pi$  stacking with Trp82.

- . e docking investigation showed that bambuterol hydrochloride depicted higher binding interactions than thio. avin T. Still, the common residues like Trp82 which was able to form ionic and  $\pi$ -cation interactions. Additionally, ionic interaction was observed between BMB oxygen atom and Ser198, ionic bond with Glu197 and BMB ammonium nitrogen and amide-  $\pi$  interaction between BMB aromatic ring and Gly116 (Table 8). All of which justify the lower binding score and higher affi ty of bambuterol than thio. avin T towards the butyrylcholinesterase enzyme.
- ese interactions suggest that BMBH has a high affi ty for BChE, which may impact its inhibitory potential against the enzyme. This interaction is significant because BChE is involved in the breakdown of acetylcholine, and its inhibition can enhance cholinergic transmission. BMBH's inhibition of this enzyme could lead to increased acetylcholine levels, which is benefical for treating neurodegenerative diseases such as Alzheimer's disease. This suggests that BMBH could be a promising candidate for further development as a cholinesterase inhibitor, potentially improving cognitive function in patients with cholinergic defic ts.

Secondly, to evaluate the bioavailabilty of BMBH, it was docked against Human Serum Albumin (HSA), a highly abundant multifunctional protein in the blood plasma, and compared to a well-known  $\beta_2$ -adrenergic

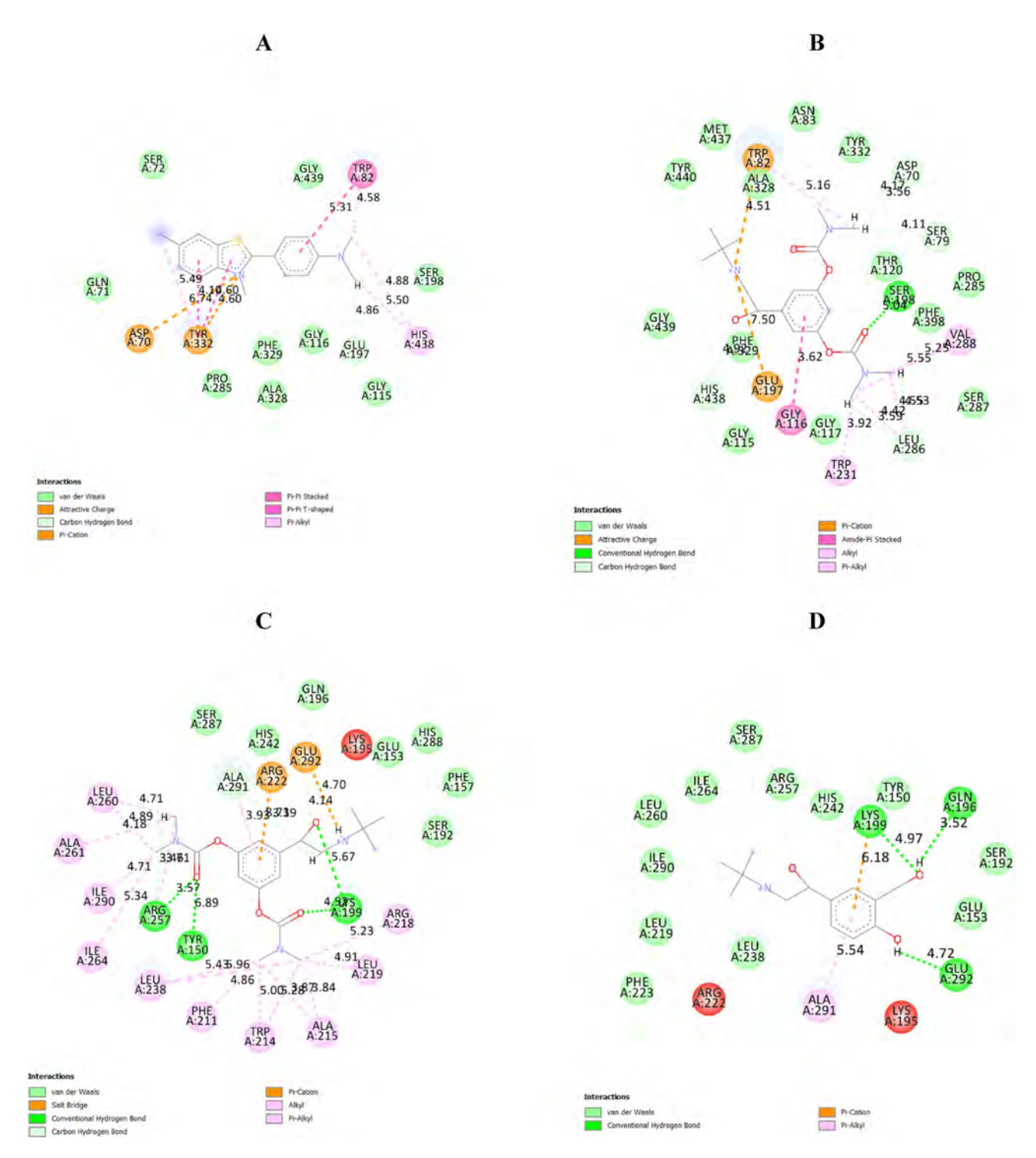


**Fig. 15**. Molecular docking analysis of thio. avine T against BChE (**A**), BMBH against BChE (**B**), BMBH against HSA (**C**), and salbutamol against HSA protein (**D**).

agonist (salbutamol). HSA plays a critical role in transporting a wide range of endogenous and exogenous molecules, including drugs, metabolites, and fatty acids. Docking against HSA is important as many natural compounds, such as plant-derived bioactives, bind to HSA. Docking studies can help assess whether a compound can efficiently utilize this transport mechanism to reach its target tissues. . e interaction of BMBH with the HSA binding site results in a high binding energy of -8.32 kcal/mol, which provides insight into the compound's high binding affictly. The eprincipal interactions are observed in Fig. 15C: 3 hydrogen bonds with Lys199, Tyr150, and Arg257, the salt bridge with Glu292 and Pi-cation interaction between the ligand's aromatic ring with Arg222. Furthermore, hydrophobic interactions contributed to the ligand's high binding affictly, with hydrophobic residues observed to be involved in this interaction. On the other hand, less binding affictly is

Receptor	Compound	Energy score (S) (kcal/mol)	Amino acids involved in interaction
			Asp70
	Thi . avine T	- 5.75 rmsd 1.16	Trp82
			Tyr332
BChE			Trp82
		7.00	Gly116
	Bambuterol	-7.99	Glu197
			Ser198
			Lys199
			Tyr150
		-8.32	Arg257
HSA			Glu292
нѕа			Arg222
			Glu196
	Salbutamol	-6.35	Lys199
			Gln292

**Table 8**. Energy scores (kcal/mol) and interactions for bambuterol hydrochloride, thio. avine T and salbutamol against BChE and HAS.

observed between  $\beta_2$ -adrenergic agonist (salbutamol) and HSA forming a  $\pi$ -cation interaction with Lys199 and 3 H-bonds with Glu196, Lys199, and Gln292 (Fig. 15D).

Th s di. erence in the binding affi ties against HSA protein indicates that BMB might have a longer duration of action compared to other  $\beta_2$ -agonists while salbutamol exhibits quicker onset but shorter action.

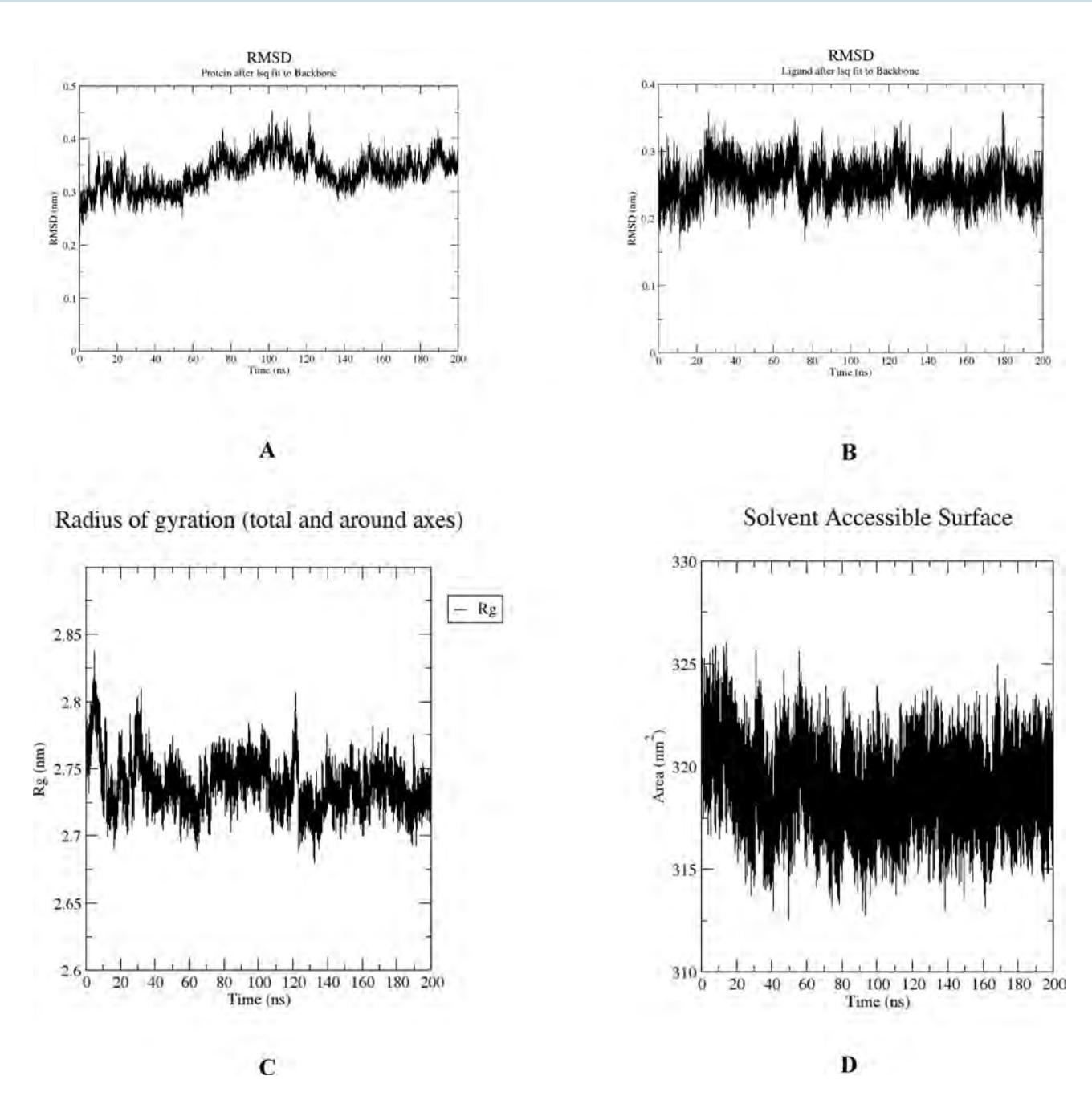
#### Molecular dynamics analysis

e results presented highlight the dynamic behavior of the HSA protein upon binding with BMBH, as well as the behavior of the ligand itself throughout the 100 ns simulation trajectory. Firstly, focusing on the RMSD of the HSA protein upon BMBH binding, it is evident that there is a stable . uctuation observed over the course of the simulation. . e average RMSD value of approximately 0.35 nm indicates that the protein maintains a relatively stable conformation, suggesting that the binding event with BMBH does not induce signifi ant structural changes in the protein (Fig. 16A). Th s stable . uctuation suggests that the protein remains in a conformation close to its initial state, with minor deviations. . ese deviations occur due to inherent flex bility or environmental factors. Th s indicates that HSA undergoes only minor structural deviations, suggesting that BMBH binding does not signifi antly alter the overall conformation of HSA. Th s stability implies that BMBH . ts well within its binding pocket without inducing large-scale structural changes.

Conversely, the RMSD of the ligand demonstrates a similar pattern throughout the simulation trajectory. Additionally, the ligand's RMSD exhibits discernible oscillatory behavior, especially a. er 20ns of the simulation (Fig. 16B). . ese steady . uctuation in the ligand's RMSD suggests a stable binding and interaction within the binding site of HSA, confi ming that BMBH remains consistently bound within the binding site without excessive movement or displacement.

- . e evaluation of the protein backbone's compactness, assessed through radius of gyration (Rg) analysis, provides insights into the overall structural stability of the complex. . e observed low oscillation in Rg , particularly noticeable a. er about 20 ns of the simulation, suggests high compactness of the protein backbone over time (Fig. 16C). Furthermore, we assessed the solvent-accessible surface area (SASA) of the protein throughout the simulation to gauge its stability in the simulated environment. . e SASA measurements corroborate the stability observed in the protein RMSD analysis, showing a consistent oscillation between 315 and 325 nm². This stable oscillation suggests that the protein maintains its exposed surface area to the surrounding solvent molecules without signifi ant perturbations, supporting the notion of a dynamically stable protein–ligand complex complex despite ligand binding (Fig. 16D).
- . e lack of major . uctuations in RMSD and SASA collectively indicate that BMBH remains securely positioned within its binding pocket throughout the  $200\,\mathrm{n}\,\mathrm{s}$  simulation. . ese fi dings suggest that BMBH-HSA binding is stable over time, supporting its pharmacokinetic relevance in terms of drug transport and bioavailability.

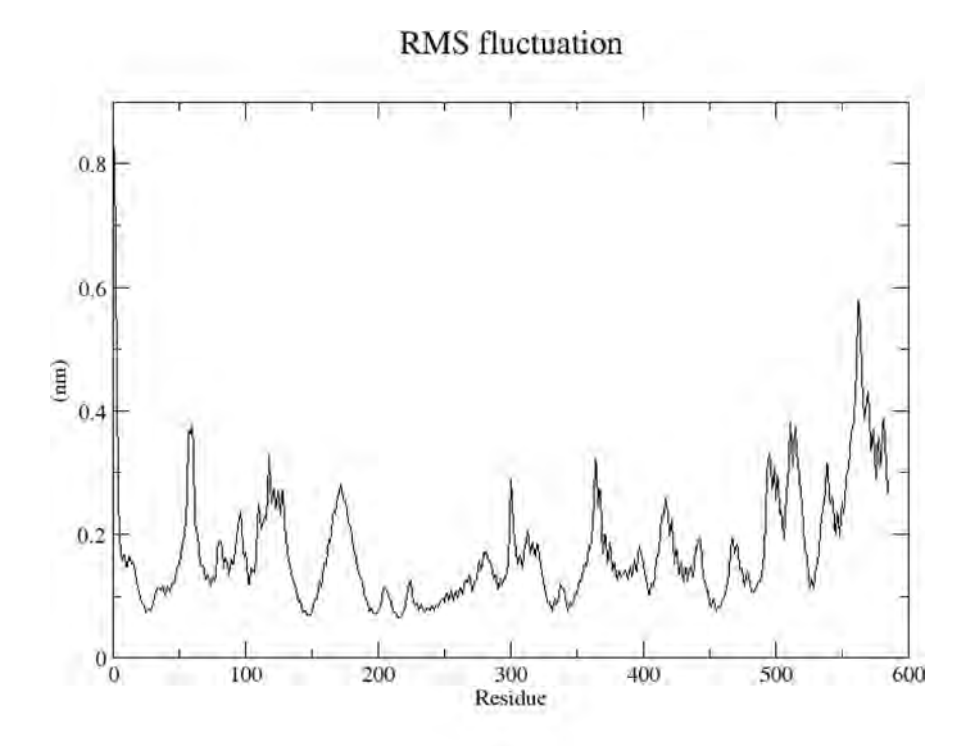
To further evaluate the stability of the complexes, the root mean square . uctuation (RMSF) of the backbone residues was calculated, with the aim of assessing the rigidity and flex bility of residues throughout the 200 ns molecular dynamics (MD) simulation. As illustrated in Fig. 17A, the complex exhibits comparable RMSF patterns, with residues engaged in ligand interactions demonstrating minimal . uctuation (<0.2 nm), such as Tyr150, Lys199, and Arg222. . ese residues are aligned with the residues involved in the interaction of BMBH with the HSA binding pocket, as reported in our docking study. Also, the number of H-bonds formed during the 200 ns trajectory confi ms that at least 3–4 H-bonds are stable throughout the simulation which aligns with the docking results (Fig. 17B).



**Fig. 16.** Structural dynamics of HSA RMSD (**A**), BMBH RMSD (**B**), complexes radius of gyration (**C**), and SASA (**D**) calculated during the 200 ns of MD trajectories.

#### Conclusion

. e structural properties of the BMBH compound were confi med using FT-IR, UV-vis, XRD, and SEM spectra. Computed vibrational frequencies of methyl groups closely matched the experimental FT-IR spectrum. A reduced HOMO-LUMO energy gap suggests charge transfer interactions, indicating NLO activity. Topological analyses (AIM, NBO, ELF, RDG) revealed hydrogen and halogen bonding characteristics, while the MEP map highlighted oxygen and chlorine as regions of negative potential. Mulliken charge analysis showed similar positive charges for all methyl hydrogen atoms. Adsorption studies on a G raphene surface demonstrated e. ective interactions with the hydrogen of HCl and methyl groups on the electron-rich surface, with a binding energy of – 31.22 kcal/mol, suggesting hydrogen storage potential. A validated docking setup was employed to examine the ligand-receptor interactions and binding mechanisms of bambuterol (binding score = -- 7.99 kcal/mol) with the dementia-related enzyme butyrylcholinesterase, identifying it as a p otential inhibitor. Th s inhibition will lead to increased acetylcholine levels, which is relevant for conditions like Alzheimer's disease and other neurodegenerative disorders. RMSD, RMSF, radius of gyration, and H-bond parameters exported from molecular dynamics simulation support the notion of a dynamically stable protein-ligand complex.



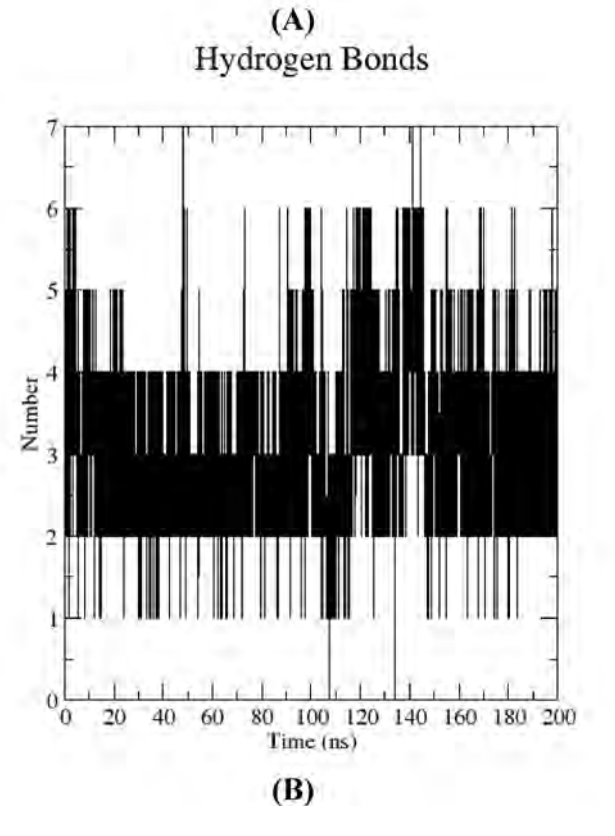


Fig. 17. Structural dynamics calculated during the 200 ns of MD trajectories; root mean square . uctuation (RMSF) of protein backbone ( $\bf A$ ), number of H-bonds formed between HSA and BMBH ( $\bf B$ ).

#### Data availability

. e datasets presented in this study can be available from the corresponding author on reasonable request.

Received: 21 February 2025; Accepted: 26 May 2025

Published online: 20 June 2025

#### References

- 1. Wen, H., Jung, H. & L i, X. Dr ug delivery approaches in addressing clinical pharmacology-related issues: Opportunities and challenges. AAPS J. 17(6), 1327–1340. https://doi.org/10.1208/s12248-015-9814-9 (2015).
- Kochkina, N. & Terekhova, I. Design of dosage forms with improved biopharmaceutical properties. *Pharmaceutics* 16(1), 69. https://doi.org/10.3390/pharmaceutics16010069 (2024).
- 3. Abdelrehim, E. S. M. & El-Sayed, D. S. Synthesis, screening as potential antitumor of new poly heterocyclic compounds based on pyrimidine-2-thiones. *BMC Chem.* https://doi.org/10.1186/s13065-022-00810-4 (2022).
- 4. Maheshwari, S., Singh, A., Varshney, A. & Sharma, A. Advancing oral drug delivery: . e science of fast dissolving tablets (FDTs). *Intell. Pharm.* https://doi.org/10.1016/j.ipha.2024.01.011 (2024).
- Dash, A. K. Drug, Dosage Form, and Drug Delivery Systems. In *Pharmaceutics* 223–238 (Elsevier, 2024). https://doi.org/10.1016/ B978-0-323-99796-6.00020-5.
- Alkhafaji, A. A. Recent perspective on polymeric semimetal (Si, Ge and As) and nonmetal (N and P) doped C70-fullerene system: Comparative electronic, dynamic behavior and chemotherapy docking with ADMET analysis. J. Organomet. Chem. 1022, 123417–123417. https://doi.org/10.1016/j.jorganchem.2024.123417 (2024).
- Albertson, T. E., Chenoweth, J. A., Pearson, S. J. & Murin, S. e pharmacological management of asthma-chronic obstructive pulmonary disease overlap syndrome (ACOS). Exp. Opin. Pharmacother. 21(2), 213–231. https://doi.org/10.1080/14656566.2019. 1701656 (2020).
- 8. Yang, A., Yu, G., Wu, Y. & Wang, H. Role of  $\beta$ 2-adrenergic receptors in chronic obstructive pulmonary disease. *Life Sci.* 265, 118864. https://doi.org/10.1016/j.lfs.2020.118864 (2021).
- 9. Nyberg, L. et al. Pharmacokinetics of bambuterol in healthy subjects. *Br J Clin Pharmacol.* 45(5), 471–478. https://doi.org/10.1046/j.1365-2125.1998.00695.x (1998).
- 10. Persson, G., Baas, A., Knight, A., Larsen, B. & Olsson, H. One month treatment with the once daily oral beta 2-agonist bambuterol in asthmatic patients. *Eur. Respir. J.* **8**, 34–39 (1995).
- 11. Cazzola, M. et a l. Oral bambuterol compared to inhaled salmeterol in patients with partially reversible chronic obstructive pulmonary disease. *Eur. J. Clin. Pharmacol.* **54**, 829–833 (1999).
- 12. Waldeck, B. Beta-adrenoceptor agonists and asthma-100 years of development. Eur. J. Pharmacol. 445(1-2), 1-12. https://doi.org/10.1016/s0014-2999(02)01728-4 (2002).
- 13. Sitar, D. S., Warren, C. P. & Aoki, F. Y. Pharmacokinetics and pharmacodynamics of Bambuterol, a long-acting bronchodilator pro-drug of terbutaline, in young and elderly patients with asthma. *Clin. Pharmacol.* er. 52(3), 297–306. https://doi.org/10.1038/clpt.1992.145 (1992)
- 14. Mostafa, N. M., Badawey, A. M. & Abd, E.-A. Polymeric matrix membrane sensors for stability- indicating potentiometric determination of bambuterol hydrochloride and its metabolite terbutaline. *J. Appl. Pharm. Sci.* 01(05), 191–197 (2011).
- 15. Cao, G. et a l. Highly enantioselective synthesis, crystal structure, and circular dichroism spectroscopy of (R)-bambuterol hydrochloride. *Chirality* 20(7), 856–862. https://doi.org/10.1002/chir.20558 (2008).
- Khalil, M. M., Abdel Moaty, S. A. & Korany, M. A. Carbon nanotubes based potentiometric sensor for determination of bambuterol hydrochloride: Electrochemical and morphology study. Sens. Actuators B Chem. 273, 429–438. https://doi.org/10.1016/j.snb.2018 .06.060 (2018).
- 17. Sitar, D. S. Clinical pharmacokinetics of bambuterol. *Clin. Pharmacokinet.* **31**(4), 246–256. https://doi.org/10.2165/00003088-199 631040-00002 (1996).
- Buya, A. B., Beloqui, A., Memvanga, P. B. & Préat, V. Self-nano-emulsifying drug-delivery systems: From the development to the current applications and challenges in oral drug delivery. *Pharmaceutics* 12(12), 1194. https://doi.org/10.3390/pharmaceutics1212 1194 (2020).
- 19. Mahmood, A. & B ernkop-Schnürch, A. S EDDS: A game changing approach for the oral administration of hydrophilic macromolecular drugs. *Adv. Drug Deliv. Rev.* 142, 91–101. https://doi.org/10.1016/j.addr.2018.07.001 (2019).
- Nasiri, S. et al. Modifi d Scherrer equation to calculate crystal size by XRD with high accuracy, examples Fe<sub>2</sub>O<sub>3</sub>, TiO<sub>2</sub> and V<sub>2</sub>O<sub>5</sub>.
   *Nano Trends* 3, 100015. https://doi.org/10.1016/j.nwnano.2023.100015 (2023).
- 21. Frisch, M.J. et al. Gaussian 09, Revision A.02. (Gaussian Inc., Wallingford, 2016).
- 22. El, S., Khalil, T. E. & E lbadawy, H. A. R ational and experimental investigation of antihypotensive midodrine-Fe(III) complex: Synthesis, spectroscopy, DFT, biological activity and molecular docking. *J. Mol. Struct.* https://doi.org/10.1016/j.molstruc.2024.13 8421 (2024).
- El-Sayed, D. S., Sinha, L. & Soayed, A. A. Experimental and theoretical quantum chemical studies of 2-(2-acetamidophenyl)-2-oxo-N-(pyridin-2-ylmethyl)acetamide and its copper(II) complex: molecular docking simulation of the designed coordinated ligand with insulin-like growth factor-1 receptor (IGF-1R). BMC Chem. 18, 112. https://doi.org/10.1186/s13065-024-01217-z (2024).
- Goerigk, L. A Comprehensive Overview of the DFT-D3 London-Dispersion Correction 195–219 (Elsevier eBooks, Netherlands, 2017). https://doi.org/10.1016/b978-0-12-809835-6.00007-4.
- Moellmann, J. & Grimme, S. DFT-D3 study of some molecular crystals. J. Phys. Chem. C 118(14), 7615–7621. https://doi.org/10.1 021/jp501237c (2014).
- 26. Lu, T. & Chen, F. Multiwfn: A multifunctional wavefunction analyzer. J. Comput. Chem. 33(5), 580 (2012).
- 27. Dennington R., Keith T. & Millam J. Gauss View Version 6.1 (Semichem Inc., Shawnee Mission, KS (2016)
- Ghuman, J. et al. Structural basis of the drug-binding specific ty of human serum albumin. J. Mol. Biol. 353(1), 38–52. https://doi. org/10.1016/j.jmb.2005.07.075 (2005).
- 29. Morris, G. M. et a l. AutoDock4 and AutoDockTools4: Automated docking with selective receptor flex bility. *J. Comput. Chem.* 30(16), 2785–2791. https://doi.org/10.1002/jcc.21256 (2009).
- Huey, R., Morris, G. M. & Forli, S. Using AutoDock 4 and AutoDock vina with AutoDockTools: A tutorial. Scripps Research Inst. Mol. Graph. Lab. 10550(92037), 1000 (2012).
- 31. Kollman, P. A. A method of describing the charge distribution in simple molecules. J. Am. Chem. Soc. 100(10), 2974-2984 (1978).
- 32. Elbadawy, H. A. et al. Zinc(II)-facilitated nucleophilic addition on N-(4-chlorophenyl) carbon hydrazonoyl dicyanide and hybrid complex formation: X-ray, spectral characteristics, DFT, Molecular docking, and biological studies. *Appl. Organomet. Chem.* https://doi.org/10.1002/aoc.6793 (2022).
- 33. Jejurikar, B.L. & S.H. Rohane. Drug designing in discovery studio (2021).
- 34. Van Der Spoel, D. et al. GROMACS: Fast, flex ble, and free. J. Comput. Chem. 26(16), 1701-1718 (2005).
- 35. Lee, J. et al. CHARMM-GUI input generator for NAMD, GROMACS, AMBER, OpenMM, and CHARMM/OpenMM simulations using the CHARMM36 additive force fi ld. *Biophys. J.* 110(3), 641a (2016).

- 36. Zhu, S. Validation of the generalized force fi lds GAFF, CGenFF, OPLS-AA, and PRODRGFF by testing against experimental osmotic coeffici t data for small drug-like molecules. J. Chem. Inf. Model. 59(10), 4239-4247 (2019)
- Pandey, A. et al. Structural characterization of polycrystalline thin. Ims by X-ray di. raction techniques. J Mater Sci: Mater Electron 32, 1341–1368. https://doi.org/10.1007/s10854-020-04998-w (2021).
   Glendening, E. D., Landis, C. R. & Weinhold, F. NBO 6.0: Natural bond orbital analysis program. J. Comput. Chem. 34(16),
- 1429-1437. https://doi.org/10.1002/jcc.23266 (2013).
- 39. Jacquemin, D. & Perpète, E. A. On the basis set convergence of TD-DFT oscillator strengths: Dinitrophenylhydrazones as a case study. J. Mol. Struct. (. oechem) 804(1-3), 31-34. https://doi.org/10.1016/j.theochem.2006.10.012 (2007).
- 40. El-Sayed, D. S. et a l. Structural and topological analysis of thiosemicarbazone-based metal complexes: computational and experimental study of bacterial bio. lm inhibition and antioxidant activity. BMC Chem. 19, 24. https://doi.org/10.1186/s13065-02 4-01338-5 (2025).
- 41. Amati, M., Stoia, S. & Baerends, E. J. . e electron affi ty as the highest occupied anion orbital energy with a suffici tly accurate approximation of the exact Kohn-Sham potential. J. Chem. eory Comput. 16(1), 443-452. https://doi.org/10.1021/acs.jctc.9b009
- 42. Bulat, F. A., Murray, J. S. & Politzer, P. Identifying the most energetic electrons in a molecule: . e highest occupied molecular orbital and the average local ionization energy. Comput. eor. Chem. 1199, 113192. https://doi.org/10.1016/j.comptc.2021.113192 (2021).
- 43. Politzer, P. & Truhlar, D. G. Chemical Applications of Atomic and Molecular Electrostatic Potentials (Springer Nature, Boston, 1981). https://doi.org/10.1007/978-1-4757-9634-6.
- 44. Pathak, R. K. & Gadr e, S. R. Maximal and minimal characteristics of molecular electrostatic potentials. J. Chem. Phys. 93(3), 1770-1773. https://doi.org/10.1063/1.459703 (1990).
- 45. Murray, J. S. & Politzer, P. e electrostatic potential: An overview. WIREs Comput. Mol. Sci. 1(2), 153-163. https://doi.org/10.100 2/wcms.19 (2011).
- 46. Ibraheem, H. H., I ssa, A. A. & E l-Sayed, D. S. Structural behavior and surface layer modifi ation of (E)-N'-((1H-indol-3-Yl) methylene)-4-chlorobenzohydrazide: spectroscopic, DFT, biomedical activity and molecular dynamic simulation against Candida albicans receptor. J. Mol. Struct. https://doi.org/10.1016/j.molstruc.2024.138484 (2024).
- 47. Johnson, E. R. et al. Revealing noncovalent interactions. J. Am. Chem. Soc. 132(18), 6498-6506. https://doi.org/10.1021/ja100936w (2010)
- 48. Humphrey, W., Dalke, A. & Schulten, K. VMD: Visual molecular dynamics. J. Mol. Graph. 14(1), 33-38. https://doi.org/10.1016/0 263-7855(96)00018-5 (1996).
- 49. Reeda, V. S. et a l. Comprehensive analysis of 2,5-dimethyl-1-(naphthalen-1-yl)-1H-pyrrole: X-ray crystal structure, spectral, computational, molecular properties, docking studies, molecular dynamics, and MMPBSA. J. Mol. Struct. 1321(3), 140062. https: //doi.org/10.1016/j.molstruc.2024.140062 (2025).
- 50. Divya, P. et al. Structural insights and ADMET analysis of CAFI: hydrogen bonding, molecular docking, and drug-likeness in renal function enhancers. BMC Chem. 19, 36. https://doi.org/10.1186/s13065-025-01383-8 (2025).
- 51. Bader, R. F. W. Atoms in molecules. Acc. Chem. Res. 18(1), 9-15. https://doi.org/10.1021/ar00109a003 (1985).
- 52. Koch, U. & Popelier, P. L. A. Characterization of C-H-O hydrogen bonds on the basis of the charge density. J. Phys. Chem. 99(24), 9747-9754. https://doi.org/10.1021/j100024a016 (1995)
- 53. Sajan, D., Joe, H., Jayakumar, V. & Zaleski, J. Structural and electronic contributions to hyperpolarizability in methyl p-hydroxy benzoate. J Mol Struct 785, 43-53 (2006).
- 54. Sun, Y.-X. et al. Experimental and density functional studies on 4-(3,4-dihydroxybenzylideneamino)antipyrine, and 4-(2,3,4-trihydroxybenzylideneamino)antipyrine. J. Mol. Struct. Chem: eochecm 904(1-3), 74-82. https://doi.org/10.1016/j.th eochem.2009.02.036 (2009).
- 55. Srivastava, R. et al. A combined experimental and theoretical DFT (B3LYP, CAM-B3LYP and M06-2X) study on electronic structure, hydrogen bonding, solvent e. ects and spectral features of methyl 1H-indol-5-carboxylate. J. Mol. Struct. 1137, 725-741. https://doi.org/10.1016/j.molstruc.2017.02.084 (2017).
- 56. Issa, A. A., K amel, M. D. & El-Sayed, D. S. Depicted simulation model for removal of second-generation antipsychotic drugs adsorbed on Zn-MOF: adsorption locator assessment. J. Mol. Model 30, 106. https://doi.org/10.1007/s00894-024-05896-2 (2024).
- 57. Jyothirmai, M.V., & Singh, J. K. Computational insights into the adsorption of organic compounds on peptide surfaces. Surf. Interfaces 56, 105624. https://doi.org/10.1016/j.surfin.20 4.105624 (2024).
- Waleed, A. et al. Adsorption locator behavior of polycyclic-carbon based systems: Computational optical and dynamic properties. Russ. J. Gen. Chem. 94, 2676-2688. https://doi.org/10.1134/S107036322410013X (2024).

#### Acknowledgements

Th s work is a part of Walaa. S. S. Alblozy M.Sc. thesis. . e authors would like to thank Assiut University for the offi al, technical, and fi ancial support. . e authors also acknowledge a generous allocation of computer time granted by SHARCNET, a partner consortium in the Compute Canada national HPC platform.

#### Author contributions

W.S.S.A. made Methodology, Visualization, So. ware. Writing—original draft. D.S.E.S. did Writing—review & editing, Visualization, So. ware, Investigation, Formal analysis. R.M.M. performed Writing—review & editing, Writing—original draft, isualization, Supervision, Methodology, Investigation, Conceptualization.

#### Funding

Open access funding provided by . e Science, Technology & Innovation Funding Authority (STDF) in cooperation with . e Egyptian Knowledge Bank (EKB).

#### **Declarations**

#### Competing interests

e authors declare no competing interests.

#### Additional information

**Correspondence** and requests for materials should be addressed to D.S.E.S. or R.M.M.

**Reprints and permissions information** is available at www.nature.com/reprints.

**Publisher's note** Springer Nature remains neutral with regard to jurisdictional claims in published maps and institutional a. liations.

**Open Access** This article is licensed under a Creative Commons Attribution 4.0 International License, which permits use, sharing, adaptation, distribution and reproduction in any medium or format, as long as you give appropriate credit to the original author(s) and the source, provide a link to the Creative Commons licence, and indicate if changes were made. . e images or other third party material in this article are included in the article's Creative Commons licence, unless indicated otherwise in a credit line to the material. If material is not included in the article's Creative Commons licence and your intended use is not permitted by statutory regulation or exceeds the permitted use, you will need to obtain permission directly from the copyright holder. To view a copy of this licence, visit <a href="https://creativecommons.org/licenses/by/4.0/">https://creativecommons.org/licenses/by/4.0/</a>.

©. e Author(s) 2025